The Star Formation History and Extended Structure of the Hercules Milky Way Satellite[1]

David J. Sand,[2,3] Edward W. Olszewski,[4] Beth Willman,[5] Dennis Zaritsky,[4] Anil Seth,[3] Jason Harris,[6] Slawomir Piatek[7] and Abhijit Saha[8]

dave.j.sand@gmail.com

ABSTRACT

We present imaging of the recently discovered Hercules Milky Way satellite and its surrounding regions to study its structure, star formation history and to thoroughly search for signs of disruption. We robustly determine the distance, luminosity, size and morphology of Hercules utilizing a bootstrap approach to characterize our uncertainties. We derive a distance to Hercules of 133 ± 6 kpc via a comparison to empirical and theoretical isochrones. As previous studies have found, Hercules is very elongated, with $\epsilon = 0.67 \pm 0.03$ and a half light radius of $r_h \simeq 230$ pc. Using the color magnitude fitting package StarFISH, we determine that Hercules is old (> 12 Gyr) and metal poor ($[Fe/H] \sim -2.0$),

[1]Based on data acquired using the Large Binocular Telescope (LBT). The LBT is an international collaboration among institutions in the US, Italy, and Germany. LBT Corporation partners are the University of Arizona, on behalf of the Arizona university system; Instituto Nazionale do Astrofisica, Italy; LBT Beteiligungsgesellschaft, Germany, representing the Max Planck Society, the Astrophysical Institute of Postdam, and Heidelberg University; Ohio State University; and the Research Corporation, on behalf of the University of Notre Dame, the University of Minnesota, and the University of Virginia.

[2]Harvard Center for Astrophysics and Las Cumbres Observatory Global Telescope Network Fellow

[3]Harvard-Smithsonian Center for Astrophysics, 60 Garden Street, Cambridge MA 02138

[4]Steward Observatory, University of Arizona, Tucson, AZ 85721

[5]Haverford College, Department of Astronomy, 370 Lancaster Avenue, Haverford PA 19041

[6]Previous address: National Optical Astronomical Observatories, 950 North Cherry Avenue, Tucson, AZ 85726

[7]Department of Physics, New Jersey Institute of Technology, Newark, NJ 07102

[8]National Optical Astronomical Observatories, 950 North Cherry Avenue, Tucson, AZ 85726

with a spread in metallicity, in agreement with previous spectroscopic work. We infer a total absolute magnitude of $M_V = -5.3 \pm 0.4$. Our innovative search for external Hercules structure both in the plane of the sky and along the line of sight yields some evidence that Hercules is embedded in a larger stream of stars. A clear stellar extension is seen to the Northwest with several additional candidate stellar overdensities along the position angle of Hercules out to ∼35' (∼1.3 kpc). While the association of any of the individual stellar overdensities with Hercules is difficult to determine, we do show that the summed color magnitude diagram of all three is consistent with Hercules' stellar population. Finally, we estimate that any change in the distance to Hercules across its face is at most ∼6 kpc; and the data are consistent with Hercules being at the same distance throughout.

Subject headings:

1. Introduction

The Sloan Digital Sky Survey has proved a fruitful database for uncovering extremely low surface brightness satellites of the Milky Way (MW). Spectroscopic studies have confirmed ten recently discovered satellites to be the least luminous ($-6.5 \lesssim M_V \lesssim -2$, not including Canes Venatici I; Martin et al. 2008b), most dark matter dominated ($(M/L)_0 \gtrsim 100$) galaxies known, based on mass models that assume dynamical equilibrium (Muñoz et al. 2006; Simon & Geha 2007; Geha et al. 2009). Recent evidence that all of the MW dwarf spheroidals occupy a similar mass scale (e.g. Strigari et al. 2008; Walker et al. 2009), despite their very different luminosities and sizes, suggests that the MW satellites will provide unique clues to basic astrophysics in simple dark matter potential wells, and to the formation of the Galactic halo.

The uncertain extent to which the MW's tidal field has played a role in shaping both the kinematics and luminosity of individual MW ultra-faint (UF) satellites and their spatial distribution as a population complicates interpretation of these data. Direct morphological arguments, as well as indirect arguments based on the mass-metallicity relationship, hint that most or all of the five UF satellites with $d < 50$ kpc may have been affected by tides (Willman et al. 2006; Zucker et al. 2006; Belokurov et al. 2007; Simon & Geha 2007; Martin et al. 2008b, for Willman 1, Segue 1, Boötes II, Ursa Major II, Coma Berenices, respectively; but see Walker et al. 2009). Because these five objects are both the nearest and the very least luminous ($M_V > -4$) UF satellites, even if tides did shape all five of these they did not necessarily shape the UFs as a population. It is important to carefully investigate whether the more distant and relatively more luminous MW UFs have lost stars

to the MW's tidal field to determine the degree to which tides may have affected the UFs as a population.

Initial attempts at studying the parameterized structure of the population as a whole (Martin et al. 2008b), along with their star formation history (SFH) via color magnitude diagram (CMD) fitting techniques (de Jong et al. 2008b), have provided a basic overview of these new systems. The SFHs are broadly consistent with old (>10 Gyr) and metal-poor ([Fe/H] < -2) stellar populations, with only UMa II, CVn I and Leo T showing evidence for extended star formation. Stellar population studies of UFs can also be used to investigate the extent to which the MW's tidal field has influenced their structural properties. For example, Martin et al. (2008b) showed that the apparent deviation in some of the UFs from a symmetric distribution can be explained by shot noise, rather than requiring truly distorted morphologies. The UFs do have more elliptical morphologies on average than the MW dwarf spheroidals known prior to 2003. However, these studies are arguably limited due to their SDSS-level magnitude limit – a level at which many of the new satellites are barely detectable in the first place.

Deep, follow-up imaging studies of individual satellites, with their ability to detect many more stars than the discovery data, have provided tighter constraints on their stellar populations and structure (e.g. Coleman et al. 2007; Walsh et al. 2008; Martin et al. 2008a; de Jong et al. 2008a; Okamoto et al. 2008). However, to date these deeper studies have covered only the central regions of the UFs, leaving their outer properties unexplored. For instance, there has been no deep and wide-field mosaics around the new systems to characterize their outer structure or to search for extremely low surface brightness extensions and hyper-faint companions. Both observational and theoretical studies of the Local Group suggest that this is a potentially rich vein of research, with some MW satellites exhibiting clear substructure (e.g. Coleman et al. 2005). Others may have their own faint satellites (Belokurov et al. 2008), and stellar streams are found throughout the Local Group (e.g. Ibata et al. 1994; Belokurov et al. 2006; Grillmair 2009). These low surface brightness phenomena are expected based on simulations of structure formation in a cold dark matter-dominated universe, and can be used as tests of galaxy formation plus dark matter models (e.g. Kravtsov et al. 2004; Bullock & Johnston 2005).

The Hercules dwarf galaxy is an excellent candidate for further deep and wide-field study. An initial Large Binocular Telescope (LBT) study by Coleman et al. (2007) found Hercules has an ellipticity of $\epsilon = 0.67$, with some indication of tidal debris directly to the West of the satellite's center. Its ellipticity is remarkable, given that spectroscopic work by Simon & Geha (2007) has shown that Hercules shows no sign of internal rotation, and a velocity dispersion of $\sigma \sim 5$ km/s. It is difficult to understand how a stellar system can have

an ellipticity this large and no rotational support. One solution to this apparent paradox may be that Hercules is not in dynamical equilibrium; it may instead be severely tidally distorted. As with many of the new MW satellites, Hercules appears to be metal poor ($[Fe/H]_{Herc} \sim -2.6$), with an intrinsic $\sigma_{[Fe/H]}$ of 0.5 dex (Kirby et al. 2008). Hercules is distant, with $d = 132$ kpc (Coleman et al. 2007), and is racing away from the Milky Way at 145 km/s (Simon & Geha 2007), the highest radial velocity of the new satellites.

Here we present deep photometry of Hercules and surrounding regions with the Large Binocular Telescope (LBT). The goal is to perform a detailed analysis of both the structure and SFH of Hercules. Additionally, we systematically search for signs of extended structure both along the line of sight and in the plane of the sky via our multiple pointings. The outline of the paper is as follows. In § 2 we describe the observations, data reduction and photometry. In § 3, we derive basic properties of Hercules, including its distance, structure and SFH. We describe our techniques for searching for extended structure associated with Hercules in § 4. Finally, we discuss our results and conclude in § 5.

2. Observations and Data Reduction

Our observing strategy was to get deep, wide field B and r band imaging of the Hercules dwarf spheroidal in order to study its extended structure and SFH. For our central pointing of Hercules, we have also used V band imaging, as presented in Coleman et al. (2007). We split our imaging between fields on and adjacent to Hercules, situated roughly along the major axis. In all we obtained five fields, whose orientation is shown in Figure 1.

Observations of Hercules were, with one exception, taken during May and June 2008 during normal operations of the Large Binocular Telescope, fitted with the red and blue channel of the Large Binocular Camera (LBC; Ragazzoni et al. 2006). The B and V band images for the central Hercules field were taken during Science Demonstration Time (SDT) and were presented in Coleman et al. (2007). During this period, only the blue channel of the LBC was employed, but otherwise the camera set up was identical. LBC consists of two nearly identical prime focus imagers, one for each of the LBT's 8.4 meter mirrors, with one optimized for blue and one for red wavelengths. Each camera has four 2048×4608 pixel CCDs, sampled at 0.23 arcsec/pixel and a ∼23'×23' field of view.

For each of our fields, we sought six 300s dithered exposures in both bands. After experimentation, we found that we could improve our point spread function (PSF) photometry via DAOPHOT (Stetson 1994) by including only the best four or five out of six frames in the analysis, and did so when necessary. This was due either to a strongly variable PSF during

an imaging sequence, or a slightly out of focus frame. Neither of these issues effected the ultimate quality of our reduced data, once it was properly culled. A summary of observations can be found in Table 1.

2.1. Data Reduction

Basic image reductions were performed in two parts and the process was identical for the B, V and r bands. First, initial reductions were executed using the *mscred* mosaic data reduction system in IRAF. This initial script trims and subtracts the overscan region, applies an additional bias subtraction to remove structure seen in the bias exposures, flat-fields the data and rejects cosmic rays in each individual exposure using the LACOSMIC task (van Dokkum 2001). Saturated objects were masked along with a growth radius of three pixels. A $\sim$1k×1k region in the extreme southwest corner of the red channel image array was excised due to poorer image quality, greatly improving overall point source photometry fits while only negligibly impacting the total area studied. Flat fields were generated by median combining flux-scaled twilight flats. An exposure weight map is calculated by combining the normalized flat field and the bad pixel map generated via cosmic ray rejection. This weight map is fed into the script which performs the next steps of the reduction process, and is specifically used by both the astrometric correction software SCAMP and the program SWarp, which resamples and coadds the images. The weight maps are not used in the determination of point source photometry, which is discussed in § 2.2.

These flat-fielded images along with their accompanying weight maps are fed into the publicly available code SCAMP (Bertin 2006) to determine the astrometric solution. Given the $f/1.14$ focal ratio, there is significant image distortion across the field of view, and a 3rd-degree polynomial fit is utilized to correct this. The astrometric catalog used was from the sixth data release of the Sloan Digital Sky Survey (SDSS-DR6) (Adelman-McCarthy et al. 2006), and the g band was used as the reference band for the B band exposures. Final astrometric solutions were good to $\sim$0″.1 rms.

Once a good astrometric solution was found and placed into the image headers, the image resampling and coaddition software SWarp[1] is employed. The LANCZOS3 interpolation function was used for image resampling, which preserves source signal while minimizing artifacts near image discontinuities, such as saturation trails. For the image coaddition we used a weighted average of the input images, which is most appropriate for detection of faint sources.

---

[1]version 2.15.7; http://terapix.iap.fr/soft/swarp

2.2. Instrumental Photometry

Stellar photometry was performed on the final image outputs from SWARP similarly to Harris (2007), using the command line version of the DAOPHOTII/ALLSTAR package (Stetson 1994). We allowed for a quadratically varying PSF across the field when determining our model PSF. Similar to Harris (2007), we ran ALLSTAR in two passes; once on the image and then again on the image with the first round's stars subtracted, so that fainter sources can be recovered. The ALLSTAR catalogs for each imaging band were culled of outliers in χ^2 vs. magnitude, magnitude error versus magnitude and sharpness versus magnitude space to remove objects that were erroneously selected as point sources in DAOPHOT. The point source B and r catalogs (along with the V band for the central pointing) were positionally matched with a maximum match radius of $0''\!.5$. Only those sources detected in both bands (or all three bands in the central pointing) are placed into our final catalog.

2.3. Photometric Calibration and inclusion of SDSS data

Calibrating the instrumental magnitudes output by our stellar photometry analysis onto a standard photometric system was done using stars in common with SDSS-DR6[2]. For the r-band, this calibration was done by matching to point sources with $19.5 < r < 21.0$. We fit a zero-point and a color term, with a total photometric uncertainty of $\delta r \sim 0.03 - 0.04$ mag depending on the pointing. For the B band, we used the relations found by Jordi et al. (2006) to convert from SDSS magnitudes, again over point sources with $19.5 < r < 21.0$ and $19.5 < g < 21.0$. The total photometric uncertainty is $\delta B \sim 0.05$ mag. Color terms were found and eliminated in $(B - B_{LBT})$ versus $(B_{LBT} - r_{LBT})$, $(V - V_{LBT})$ versus $(B_{LBT} - V_{LBT})$ and $(r - r_{LBT})$ versus $(B_{LBT} - r_{LBT})$ space; the linear slope of these terms was 0.09, -0.03 and -0.02 mag, respectively. There were slight residual zeropoint gradients across the field of view, and it was necessary to fit a quadratic function to the zeropoint as a function of chip position to achieve the above zero-point uncertainties. This was done for each individual pointing.

When necessary, we adopted SDSS photometry directly for stars brighter than and near the saturation limit of a given LBT field (which depends both on the observing conditions and point spread function). In this case, g and r magnitudes are once again converted to B magnitudes via the relations found by Jordi et al. (2006).

All reported magnitudes are corrected for Galactic extinction with the values from the

---

Schlegel et al. (1998) dust maps, using the IDL routine DUST_GETVAL. Specifically, we used $A_B = 4.315E(B - V)$ and $A_r = 2.751E(B - V)$. Unless stated otherwise, all magnitudes reported in the remainder of this paper will be extinction corrected.

2.4. Artificial Star Tests

Artificial star tests were used to measure both our photometric errors and completeness as a function of magnitude and color, with a methodology analogous to that presented by Walsh et al. (2008). First, artificial stars are injected into the original images based on the point spread function (PSF) measured by DAOPHOT with the routine ADDSTAR. Artificial stars were placed on a regular grid with spacing between ten and twenty times the full width at half maximum, so that the overlap between artificial stars is negligible. Given the geometry of the LBC field of view, this allows for ~5000-20000 artificial stars per iteration. In order to build up sufficient statistics, 10 iterations were performed per field for a total of ~100000 artificial stars each. The r magnitude of the artificial stars is drawn randomly from 18 to 29 mag, with an exponentially increasing probability toward fainter magnitudes. The $B - r$ color is then randomly assigned over the range -0.5 to 1.5 mag, with uniform probability. The artificial star frames are run through the same photometry pipeline as the science frames, with identical χ^2, sharpness and error on the magnitude cuts. Also, a given star must be detected in both the B and r band (B,V and r in the central field) to be considered a true detection. The 50%, 90% and 95% completeness limits for each field is detailed in Table 1.

2.5. Final Hercules Catalog

The final step in preparing our Hercules photometric catalog was the combination of the individual catalogs from the five separate image pointings. Since there was some overlap between the pointings, we chose the photometry with the lower formal photometric error to put in the final catalog. We directly compared the photometry of objects detected in more than one pointing and found them to be consistent with the uncertainty in the recovered magnitudes found in our artificial star tests.

We present our full Hercules catalog in Tables 2 and 3. Table 2 focuses on our central pointing and includes our B, V, and r band magnitudes (uncorrected for extinction) with their uncertainty. We also include the extinction values derived for each star and whether or not the star was taken from the SDSS catalog and converted to B and V via the relations

of Jordi et al. (2006), rather than from our LBT data. Table 3 is similar, and includes our data from our adjacent fields, which is noted in its own separate column.

3. Hercules Properties

Figure 2 shows the CMD of stars within 5.9 arcminutes of the center of Hercules, the half light radius for an exponential profile parameterization (§ 3.2). Using this data, we will measure the distance, structural properties, and SFH of Hercules.

3.1. Distance

Most recently, the distance to Hercules has been calculated in the LBT study of Coleman et al. (2007), and was found to be 132 ± 12 kpc ($m - M = 20.6 \pm 0.2$). For completeness, along with our study of Hercules' extended structure and SFH, we reinvestigate the distance to Hercules.

We proceed by comparing Hercules' CMD with empirical globular cluster fiducials and theoretical isochrones utilizing a bootstrap technique analogous to Walsh et al. (2008). We use four empirical fiducials from Clem et al. (2008) recently imaged in Sloan g' and r': M92, M3, M13 and M71 which span a range of metallicity $-2.4 < [Fe/H] < -0.7$. We take $m-M$=14.60, 15.14, 14.42 and 13.71 (Paust et al. 2007; Kraft & Ivans 2003; Cho et al. 2005; Grundahl et al. 2002) and $E(B-V)$=0.022,0.013,0.017,0.308 for the four clusters respectively. The Clem et al. (2008) fiducials were converted from g',r' to g,r using the transformation of Rider et al. (2004) and then to B,r using the transformation of Jordi et al. (2006). Besides these four empirical fiducials, theoretical isochrones were taken from Dotter et al. (2008) and Girardi et al. (2004). The two Dotter isochrones used were for a $[Fe/H] = -2.49$ and $[Fe/H] = -1.5$, 15 Gyr stellar population, while the Girardi isochrones were for a $[Fe/H] = -2.3$ and $[Fe/H] = -1.7$ 15 Gyr stellar population. The following technique is robust only if the underlying stellar population of Hercules is old, which we discuss further in § 3.3. Note that if Hercules has a spread in metallicities, as indicated by Kirby et al. (2008) and for which we present evidence in § 3.3, then the distance modulus will have an additional uncertainty, which we will try to quantify later in this section.

We include all stars within r_h=5.9' of the centroid of Hercules, taken via the best-fitting exponential profile (see § 3.2 and Table 4), down to $r = 25.5$ in our analysis. Restricting ourselves to stars with $r < 24.5$ does not change the result. To determine the best fit distance modulus, each fiducial is stepped through 0.025 magnitude intervals in $(m - M)$

from 19.5 to 21.5, noting the number of stars consistent with (taking into account photometric uncertainties) that of the fiducial. To account for background/foreground contamination, we then calculate the same numbers for stars in an equal area box 12 arcminutes north of the centroid of Hercules (since Hercules is oriented nearly East-West and is highly elongated, there should be little Hercules contamination at this position) and subtract it from the Hercules-centered result. The best fit distance modulus is that which maximizes the number of Hercules stars.

The best-fit distance moduli for the M92, M3, M13, and M71 fiducials are 20.625, 20.375, 20.25 and 20.925, with 894, 843, 850 and 877 stars, respectively. Note that if we perform a similar analysis on the $B - V$ versus V CMD, we achieve a nearly identical result, with the M92 CMD being the best fit with a distance modulus of 20.60. For the theoretical isochrones, the Dotter $[Fe/H] = -2.49$ 15 Gyr isochrone yields a 20.60 distance modulus with 895 stars while the Dotter $[Fe/H] = -1.5$ 15 Gyr isochrone has a distance modulus of 20.2 and 819 stars. Likewise, the Girardi $[Fe/H] = -2.3$, 15 Gyr isochrone is at a distance modulus of 20.65 with 892 stars and the Girardi $[Fe/H] = -1.7$, 15 Gyr isochrone is at 20.2 with 842 stars.

Clearly, old and metal poor isochrones provide the best fit to the Hercules CMD, with the M92, Dotter $[Fe/H] = -2.49$ and Girardi $[Fe/H] = -2.3$ isochrones all giving similar results. In Figure 3, we present a Hess diagram of the central r_h=5.9' of Hercules with background subtracted, along with the M92 fiducial adjusted to $(m - M)$=20.625. The fit is excellent, and nearly identical for the two good theoretical isochrones as well. As an exercise, if we force isochrones with $[Fe/H] \sim -1.5$ to the best fit distance modulus of the M92 fit, as we do for illustrative purposes in Figure 4 using the M13 isochrone, we see that they provide a poorer match to the Hercules CMD, but we can not rule out that a fraction of the Hercules CMD belongs to a slightly more metal rich population – a fact we will return to in § 3.3.

For most of this work we choose to adopt the best-fit distance modulus found for the empirical globular fiducial, M92, of $(m - M)$=20.625. However, in § 3.3, where we attempt to fit the star formation history of Hercules using a set of theoretical isochrones from Girardi et al. (2004) to the observed CMD, we use the best fit Girardi $[Fe/H] = -2.3$ distance modulus of 20.65.

3.2. Structural Parameters

It is traditional to fit the surface density profile of both globular clusters and dSphs to King (King 1966), Plummer (Plummer 1911), and exponential profiles. While real MW

satellites have a complexity that is difficult to characterize with parameterized models, it is nonetheless important to facilitate comparisons with other observational studies and for studies of the faint MW satellites as a population (e.g., Martin et al. 2008a). We fit all three profiles to the stellar distribution of Hercules:

$$\Sigma_{King}(r) = \Sigma_{0,K} \left(\left(1 + \frac{r^2}{r_c^2} \right)^{-\frac{1}{2}} - \left(1 + \frac{r_t^2}{r_c^2} \right)^{-\frac{1}{2}} \right)^2 \qquad (1)$$

$$\Sigma_{Plummer}(r) = \Sigma_{0,P} \left(1 + \frac{r^2}{r_P^2} \right)^{-2} \qquad (2)$$

$$\Sigma_{exp}(r) = \Sigma_{0,E} \exp \left(-\frac{r}{\alpha} \right) \qquad (3)$$

where r_P and α are the scale lengths for the Plummer and exponential profiles and r_c and r_t are the King core and tidal radii, respectively. For the Plummer profile, r_P equals the half-light radius r_h, while for the exponential profile $r_h \approx 1.668\alpha$. For this investigation, we use all stars in the central field of Hercules which are consistent with the $(m - M)$=20.625 M92 fiducial, taking into account our photometric uncertainties. The four outlying fields were not used due to their different depths and completeness. For the King profile, there is a degeneracy between the truncation radius and the background surface density. We thus fix the background value to the average of that found for the Plummer and exponential profiles for our King profile fits (e.g. Walsh et al. 2008).

We use a maximum likelihood (ML) technique for constraining structural parameters similar to that of Martin et al. (2008a), and point the reader to that work for further details concerning the expression of the likelihood function. Whereas Martin et al. (2008a) use an iteratively refined grid to find the ML, we use the amoeba simplex algorithm (Press et al. 1988), restarted five times in order to ensure that the ML is reached, although it generally converges after three restarts. Including the central position of Hercules, α_0 and δ_0, position angle (θ), and ellipticity (ϵ) both the exponential and Plummer profiles have the same free parameters – ($\alpha_0, \delta_0, \theta, \epsilon, r_{half}, \Sigma_b$), while the King profile free parameters are ($\alpha_0, \delta_0, \theta, \epsilon, r_c, r_t$). Uncertainties on structural parameters are determined through 1000 bootstrap resamples, from which a standard deviation is calculated.

Our results are presented in Table 4. We show our best fit stellar profiles in Figure 5. Although the plotted stellar profiles are not fit to the plotted binned data points, they do show excellent agreement. For illustration and comparison with the SDSS data set (see below), we show our bootstrap histogram for our exponential profile fit for r_h in Figure 6.

These Hercules parameters are in good agreement with the LBT data of Coleman et al. (2007), with nearly identical ellipticity, position and position angle. There is some confusion as to the literature value of the half light radius of Hercules. Originally, Coleman et al. (2007) found a half light radius of $r_h = 4.37' \pm 0.29'$ via their King profile fit. Using only SDSS data, Martin et al. (2008a) found $r_h = 8.6^{+1.8}_{-1.1}$' and reported via a private communication that the half light radius of Hercules derived by Coleman et al. (2007) was $9.4 \pm 1.4'$ versus the originally reported value. We believe that our half light radius is in agreement with the SDSS-only data, which are plagued by high background and small numbers, which we discuss now.

To illustrate the gain in parameter constraints made via the deep Hercules photometry, we repeat our analysis with only the SDSS data, fitting an exponential profile. In this, we seek to mimic the analysis of Martin et al. (2008a), taking all SDSS stars within 1 degree of Hercules, and make magnitude cuts at $r < 22.0$ and $g < 22.5$, while selecting Hercules stars that are consistent with the M92 isochrone shifted to $(m - M)$=20.625. We find excellent agreement with the Hercules results of Martin et al. (2008a), albeit with larger uncertainties than their published numbers. In Figure 6, we compare the bootstrap r_h histograms from the LBT and SDSS data, although this comparison is not necessarily fair given the different fields of view that each data set was taken from. This clearly illustrates the need for deep photometry of all of the new faint MW dwarfs in order to strongly constrain their structural parameters.

As first reported by Coleman et al. (2007), the ellipticity of $\epsilon = 0.67$ is remarkable. Additionally, kinematics results of Hercules indicate a $\sigma \sim 5 km/s$, with no sign of rotation, although there is some tentative evidence that there may be some kinematic substructure (Simon & Geha 2007). Taken together, this may suggest that Hercules is disrupting or a stellar enhancement in an unidentified stream. We search for signs of extended structure in our Hercules fields in § 4.

3.3.   Star Formation History

It is important to understand the SFH and metallicity evolution of the new dwarfs, since they may provide important clues to the formation and assembly of the Local Group and may serve as a comparison to cosmological simulations. One technique for doing this is via CMD-fitting, which has already been employed to some degree to study the new SDSS dwarf galaxies (e.g., de Jong et al. 2008a,b).

Here we apply the CMD-fitting package StarFISH (Harris & Zaritsky 2001) to our pho-

tometry of stars within the half light radius (r_h=5.9') of Hercules to determine its SFH and metallicity evolution. Conceptually, StarFISH uses theoretical isochrones, taken from Girardi et al. (2004, 2002) (although in practice any set of isochrones can be used), to construct a set of artificial CMDs with different combinations of distance, age, and metallicity. Utilizing the observed photometric errors and completeness (obtained from artificial star tests in § 2.4), these theoretical CMDs can be converted into realistic model CMDs which can be compared directly to the data. Conversion of both the data and the model into Hess diagrams enable a pixel-to-pixel comparison. The best fitting linear combination of model CMDs is determined through an efficient downhill simplex algorithm, and uncertainties are evaluated by examining the parameter space about the best-fit. See Harris & Zaritsky (2001) for details of the algorithm. We should note that StarFISH has been shown to give very similar results as MATCH (de Jong et al. 2008a), another CMD-fitting software package with a slightly different implementation (Dolphin 2002; de Jong et al. 2008b).

We include isochrones with [Fe/H]=$-2.3, -1.7, -1.3, -0.7$, and -0.4 and ages between ~10 Myr and ~16 Gyr. Age bins of width $\Delta log(t)$=0.4 dex were adopted, except for the two oldest age bins at ~10 Gyr and ~14 Gyr, where the binning was $\Delta log(t)$=0.3 dex. We have included a 'foreground' CMD, taken from a region 10 arcminutes north of the center of Hercules measuring 16 by 7 arcminutes, in order to correct for contamination by foreground stars.

Two CMDs were fit simultaneously; $B-V$ versus V and $B-r$ versus r. Stars with colors in the range $-0.5 < B-V < 1.5$ and $-0.5 < B-r < 1.5$ were fit. The magnitude range included all stars brighter than $r = 26$ and $V = 26$. The Hess diagram bin size was 0.1 in magnitude and 0.1 in color. We assume a Salpeter initial mass function and a binary fraction of 0.5. These stars were taken from our final three band Hercules catalog, and so have already been corrected for foreground extinction with the dust extinction maps of Schlegel et al. (1998). We have chosen to fix the distance modulus in the code to $m - M = 20.65$, the best distance modulus found for the Girardi ischrones in § 3.1, although our results our robust with respect to this assumption (see below).

The best-fit StarFISH solution is shown in Figure 7, with a comparison of the best-fit model to the data shown in Figure 8. Note that bins with only error bars should be considered upper limits. We find that Hercules is old (> 12 Gyr) and metal poor, although there is an intrinsic spread in metallicity, with both $[Fe/H] = -2.3$ and -1.7 populations contributing to the SFH. The best fit includes 1045 Hercules stars in the central 5.9'. There has been negligible star formation for the last 12 Gyr. This general result is robust with respect to our chosen distance modulus. If we fix the distance modulus to 20.55 and rerun StarFISH, we get a similar mix of metal poor populations but with a larger fraction of the

ancient star formation coming from the $[Fe/H] = -1.7$ bin. Likewise, if we fix the distance modulus to 20.75, then Hercules has a SFH which consists of only the $[Fe/H] = -2.3$ stellar population.

Recent spectroscopic results in Hercules have also measured a spread in metallicity. Medium resolution spectroscopy of 22 red giant branch stars in Hercules has indicated that it is very metal poor, $\langle[Fe/H]\rangle=-2.58$ with a spread of $\sigma_{[Fe/H]} = 0.51$ (Kirby et al. 2008). Note that, if this is true, the Girardi isochrones are not available for the most metal-poor half of the Hercules distribution. High resolution spectra of two Hercules stars was presented in Koch et al. (2008), both of which were at $[Fe/H]=-2.0$, which reinforces the spread in Hercules metallicities.

While it is safe to say that Hercules is old and metal poor, there are several reasons that the model and observed CMDs will never match perfectly (Figure 8). The first has to do with the theoretical isochrones, which are excellent for determining general properties of stellar systems, but do have systematic variations with respect to empirical isochrones (e.g., Girardi et al. 2004). For instance, Girardi et al. (2004) note that there is a systematic offset in color of $\sim$0.1 mag below the main sequence turn off between SDSS CMDs of Pal 5 and their theoretical isochrones. They conclude that this may be due to a real color shift in the model. A similar offset in our V versus $B - V$ CMD could be responsible for our residuals in the Hess diagram in Figure 8. In addition to mild inaccuracies of the theoretical isochrones, the available models do not span the metallicity range that is apparent in the new MW dwarfs. As noted above, Kirby et al. (2008) found $\langle[Fe/H]\rangle=-2.58$ in Hercules, which is more metal poor than the available Girardi et al. (2004) isochrones allow. While the difference between a $[Fe/H]=-2.6$ and -2.3 CMD will be very small, it nonetheless may contribute to any systematic residuals. Another concern for studies of this type is proper correction for dust extinction. We have corrected for reddening using the extinction maps of Schlegel et al. (1998), but this may not be perfect, given the beam size of $\sim$6.1' in these maps. Since this is roughly the size of r_h, even though we account for reddening for each star, it is in practice impossible to do so if the extinction varies significantly on scales smaller than what we are considering here. Additionally, any dust associated with Hercules itself would not be accounted for in our reddening correction.

3.4. Absolute Magnitude

As has been pointed out by Martin et al. (2008a) and others, measuring the total magnitude of the new MW satellites is difficult due to their relatively small number of stars. To account for this 'CMD shot noise', we mimic the luminosity measurement technique of

Martin et al. in the following way.

Given the SFH solution presented in § 3.3, we created a well-populated CMD with $\sim$140,000 stars, including our completeness and photometric uncertainties. From this master CMD, we drew one thousand random realizations of the Hercules CMD with an identical number of stars as determined via our exponential profile fit (which, from Figure 5 seems to best represent the profile of Hercules) and determined the 'observed' magnitude of each realization from the luminosity of all stars above a limiting magnitude corresponding to our 90% completeness limit (switching to our 95% completeness limit effects the total magnitude by only $\sim$0.1 mag, which we add in quadrature to our overall uncertainty). Those stars fainter than this magnitude were accounted for by using luminosity function corrections derived from Dotter et al. (2008). From the one thousand realizations, we take the median as our absolute magnitude and its standard deviation as our uncertainty (Table 4). The absolute magnitude of Hercules changes by $\sim$0.03 magnitudes depending on whether we use $[Fe/H] = -2.5$ or $[Fe/H] = -1.7$ stellar populations with an age of 15 Gyr for this luminosity correction, and so use the $[Fe/H] = -2.5$ result. We also calculate Hercules' central surface brightness, $\mu_{0,V}$, assuming our exponential profile fit.

Our final $M_V = -5.3\pm0.4$ mag is $\sim$1.3 magnitudes fainter than that found by Martin et al. (2008a), although it is consistent with the discovery data of Belokurov et al. (2007) at the $1-\sigma$ level (who used deeper follow-up observations to measure integrated properties). We believe that this is due to the relatively small numbers of stars used by Martin et al.

4. Extended Structure Search

In this Section, we look for evidence of tidal tails, hyper-faint companions or other disturbances in the morphology of Hercules through unexpected enhancements in stellar density of likely Hercules members and by searching for systematic changes in its distance modulus along its face.

4.1. Morphology

First we search for signs of tidal disturbance and other Hercules features in all five LBT fields based on the morphology of Hercules' isodensity contours. All stars that are consistent, within the $1-\sigma$ photometric uncertainties, with the M92 isochrone transformed to a distance modulus of 20.625 mag are placed in $10''\times10''$ bins and spatially smoothed with three different Gaussians – with σ=1.0,1.5 and 2.0 arcminutes – in order to pick out structures of different

scales. Since each field has a different depth and completeness at a given magnitude, it is difficult to make a combined, smoothed mosaic of all fields simultaneously. We choose instead to present each field individually, with stars in the central field taken down to $r = 25.5$ mag and $r = 24.5$ mag in the other, adjacent fields – corresponding roughly to the 50% completness limit. The background level and variance was determined from the entire image via the MMM routine in IDL, which assumes that most contaminated pixel values are higher than the true background. However, since Hercules occupies the bulk of the central pointing, the background for that field was determined in a box ten arcminutes north of Hercules centroid that measures $4' \times 10'$. We present these smoothed maps in Figure 9, with the marked contours representing regions that are 3, 4, 5, 7, 10, 15 and 20 standard deviations above the background. As can be seen, there are no structures apparent in the σ=1.5 and 2.0 arcminute maps that are not also in the σ=1.0 arcminute maps. For this reason, we will focus on the σ=1.0 arcminute case for the rest of this work. Although our maps are dependent on the number of members stars above a magnitude threshold, and not directly on surface brightness, it is informative to note that the 3-σ contour of the central pointing corresponds to $\mu_r \sim 29.3$ mag arcsec^{-2}.

Given our binning and smoothing to make Figure 9, how significant is any given overdensity? To gauge this, we have used the same photometry as the input catalog, but randomized the star positions across each individual LBT field of view according to a uniform distribution. We then applied identical CMD cuts to identify likely Hercules members, binned the data and smoothed it with a Gaussian of σ=1.0 arcminute, identically to that done above. In Figure 10, we show nine such random realizations for the central Hercules field and Field 1. The random realizations of our other fields have similar characteristics. As can be seen, $3-\sigma$ overdensities are relatively common, with occasional 4 or even 5σ peaks. This will be kept in mind when examining our Hercules overdensities.

4.1.1. Inserting Artificial Remnants

We will be dealing with small numbers of stars in particular regions of these smoothed maps where there is an apparent overdensity of stars consistent with the CMD of Hercules. Visual inspection of the CMDs of these overdense regions to confirm their similarity to the Hercules CMD is difficult. To help, we have developed tools that allow us to use the SFH for Hercules determined in § 3.3, along with our artificial star tests for each of our LBT pointings, to generate artificial 'Hercules' CMDs, using the *testpop* program within the StarFISH package. These Hercules 'nuggets' can then be injected into our Hercules photometry catalog with an arbitrary spatial distribution, to see if our smoothing process

can recover them, and to determine the quality of the resulting Hess diagrams. We inject artificial Hercules nuggets with exponential profiles into our Hercules catalog, for simplicity. By varying the number of stars and the half light radius, we can compare these artificial CMDs directly with those associated with stellar overdensities in our smoothed maps and measure our sensitivity to faint remnants associated with Hercules.

As an illustration, Figure 11 shows two artificial Hercules nuggets (of 50 and 150 stars) implanted into Field 1, the field directly East of Hercules, with the properties shown in Table 5. They each have a SFH identical to that of Hercules and have a distribution randomly drawn from an exponential profile with a half light radius of 3.0 arcminutes. The 50 and 150 star nuggets result in $\sim$2.2 and 4.8 σ overdensities, after smoothing with a one arcminute Gaussian. We extract these nuggets using a circular aperture with a radius of 2 arcminutes, as illustrated in the figure, with the background Hess diagram being taken from an equal area annulus outside the aperture. As can be seen from the resulting Hess diagrams in the bottom panels of Figure 11, it is difficult to say that the 50-star nugget has a Hess diagram consistent with the Hercules CMD, although the 150-star nugget has a hint of a main sequence around $r \sim 24.2$.

In Table 5 we show the results of five such tests on each of our pointings (besides the central pointing of Hercules), where we have fixed the exponential scale radius to 3 arcminutes (116 pc at the distance of Hercules), and have simply varied the number of stars drawn from our fake Hercules CMDs generated for each pointing. We then calculated the central surface brightness and total magnitude of these nuggets as we did in § 3.4. Generally speaking, it is only for those nuggets that result in overdensities $\gtrsim 3\sigma$ where the beginning of a main sequence can be seen in the resulting Hess diagrams, and so it is this limit that we adopt when investigating the candidate stellar overdensities in our fields. Additionally, it is clear that the more stars that are used in constructing our Hess diagrams, the clearer any signal will be, and so we sum these overdensities when we can.

Table 5 is only illustrative of our sensitivity to external Hercules structure, as the detection of any given nugget is subject to several random factors. For instance, we are injecting nugget stars drawn from an exponential profile with a 3 arcminute scale radius, but are only using extraction apertures with a 2 arcminute radius, which is justified upon visual inspection of Figure 11. Also, scattering of individual stars away from our CMD detection threshold due to our incorporation of results from our artificial star tests also adds a random component, leading to a natural variance in the detectability of a given nugget.

4.1.2. Hercules overdensities

We have seen, both by randomizing the spatial positions of our input photometry (Figure 10) and by implanting fake 'Hercules' nuggets into our catalogs (§ 4.1.1), that it will be extremely difficult to investigate and be reasonably assured that any given 3σ overdensity is truly associated with Hercules. We therefore focus only on the apparent 'stream' seen in the central pointing emanating from Hercules to the Northwest, coincident with the major axis, and those Hercules 3σ overdensities which are nearly projected onto the position angle of Hercules. These could plausibly be high-density knots in a tidal stream that is currently undetectable, keeping in mind that our fields adjacent to Hercules are shallower by $\sim$1 mag than our central pointing.

We present the three relevant smoothed maps in Figure 12, and have noted the regions of interest with dashed shapes. In addition to the smoothed map, we have also marked the position of candidate blue horizontal branch stars – those that are within 2σ of the 14 Gyr, [Fe/H]=-2.3 Girardi et al. (2004) isochrone – as red diamonds in Figure 12. In general, BHB stars suffer from less foreground Galactic contamination than those on the red giant branch or main sequence, and so can be a tracer of potential external structure (Belokurov et al. 2008). Note that the stream has 3 potential BHB stars, and that two out of the three proposed Hercules knots also have a candidate BHB star. There are two other BHB star candidates along the position angle of Hercules, in Field 1, which are not directly associated with either nugget. Though by no means definitive, the presence of these stars is encouraging.

First we make a background-subtracted Hess diagram of the extension to the Northwest of Hercules, using stars in the dashed box in the middle panel of the top row of Figure 12, with an equal area background taken from a region 10' north of Hercules (bottom right; Figure 12). Indeed, there appears to be a main sequence and perhaps a few RGB stars in this apparent stream, although the main sequence is thinner than our expectation given our photometric errors. Next, we have summed the stars in the three circular apertures in Fields 1 and 2 (and stars in equal area background apertures), and created a separate Hess diagram shown in the bottom left of Figure 12. This CMD is reminiscent of those found when implanting our artificial Hercules nuggets, with the beginning of a main sequence coinciding with that of Hercules apparent.

While still tentative, it is possible we are detecting the highest density features associated with a stream emanating from Hercules. If true, the 'nuggets' that we detect in our adjacent to Hercules fields can plausibly be knots analogous to those seen in the tidal stream of Palomar 5 (Odenkirchen et al. 2003). We will discuss possible implications of this scenario in § 5.

4.2. Distance modulus across the face of Hercules

Given its high ellipticity, radial velocity of ∼140 km/s away from the MW (with respect to the Galactic standard of rest), and a hint that it may contain kinematic substructure (Simon & Geha 2007), it is worth exploring whether or not Hercules is significantly elongated along the line of sight. One complication is the fact that Hercules appears to have an intrinsic spread in metallicity – as seen in spectroscopic work (Kirby et al. 2008) and confirmed by our SFH analysis – which presents a 'thicker' giant branch and main sequence than a simple single stellar population does. We keep this in mind as we go through the following analysis.

As a first test, we remeasure the distance modulus as in § 3.1, but now in two circular regions with radius 3 arcminutes on either side of Hercules' central position; see Figure 13 for an illustration. We use a background region with radius of 3 arcminutes situated 12 arcminutes north of the centroid of Hercules to account for background/foreground contamination. We focus on the M92 fiducial, which was found to be the best-fitting empirical isochrone in § 3.1. Note that splitting Hercules up into 3 circular regions with radius of 2 arcminutes give similar results, but the distance modulus bootstrap histograms are even less clearly defined, due to small number statistics. We present the result of our bootstrap analysis in Figure 13, along with background subtracted Hess diagrams of both portions of Hercules. The eastern Hercules aperture indicates that it is at $(m − M)$=20.525 mag (127 kpc), closer than the western portion and of Hercules taken as a whole $((m − M)$=20.625 mag; 133 kpc). The eastern bootstrap histogram is broad, with multiple peaks, unlike the histogram for the western portion of Hercules which is very similar to that when Hercules is taken as a whole. While this is interesting, the result must be taken with caution – despite their differences, the eastern bootstrap histogram does have significant overlap with both the western bootstrap and Hercules as a whole.

Intrigued by these results, we decided to fit a model with Hercules' distance changing linearly as a function of major axis distance, and with no binning of the data. This model is appropriate if Hercules is actually a stellar overdensity in a thin stream whose length we are observing nearly along the line of sight. We assume that the center of Hercules is at $(m − M) = 20.625$ (133.4 kpc), as found in § 3.1, and allow the observer-Hercules distance to change as a function of the major axis distance –

$$Distance(x_i) = mx_i + 133.4(kpc) \qquad (4)$$

For a given slope, m, and major axis distance for the i-th star, x_i, the presumed distance to a Hercules member is known and if its magnitude and color are consistent (to within $1 − \sigma$) with the isochrone of M92 transformed to that distance, then it is tallied. We restrict

our analysis to the central r_h=5.9', and use several identically shaped ellipses between 9-12' north of the center of Hercules as our control. Modeled in the same way, we subtract the number of stars consistent with our linear model in the background region from those found in Hercules. We choose to vary m between -2500 and 3600 pc/arcmin. The cartoon in Figure 14 illustrates our model, while the bottom panels summarize the results over 1500 bootstrap resamples.

As can be seen from the bootstrap-derived histogram in the bottom right of Figure 14, there is no clearly preferred slope. Also, the dashed histogram – which represents the slope where the background star counts corresponded to a minimum – shows that more often than not we are really just measuring the slope that corresponds to a minimum in the background rather than a true Hercules maximum. Of course, this does not mean that Hercules has no depth along the line of sight. It may just mean that our linear model for distance across Hercules is too simple and does not correspond to reality.

Despite our careful search, we find no conclusive evidence that Hercules is elongated along the line of sight. At best, we can constrain any line of sight depth to be roughly the same size as the difference between the East and West portions of Hercules, but even then the uncertainties in these two measurements overlap at the $1 - \sigma$ level. Within the half light radius, Hercules has at most a difference in distance modulus of $\sim$0.1 mag between its Eastern and Western portions, which corresponds to $\sim$6 kpc. Note that this limit is not particularly stringent, and is an order of magnitude larger than the projected size of Hercules on the sky.

5.   Discussion & Conclusions

In this work, we have presented a comprehensive imaging study of the Hercules MW satellite and surrounding regions. With this, the first very wide-field study of one of the recently discovered SDSS satellites, we have determined the stellar population and structural properties of Hercules, and have thoroughly searched for signs of extended structure.

In utilizing a ML technique analogous to that presented by (Martin et al. 2008a), we have fit the structure of Hercules to several standard parameterized models – an exponential, Plummer and King profile. We confirm that Hercules is extremely elliptical, with $\epsilon = 0.67$. Our structural parameters are consistent with those presented in the literature (e.g. Coleman et al. 2007; Martin et al. 2008a), however, we also demonstrate that data deeper than the discovery SDSS data are essential for properly characterizing the structural properties of the new satellites. For instance, using SDSS data identical to that used

by Martin et al. (2008a), along with bootstrap resampling to determine our uncertainties, we find that Hercules has a half-light radius of 7.65'±5.16'. This constraint tightens to r_h=5.91'±0.50' with our LBT data set. It is critical that all of the satellites be followed up with deep, wide-field imaging in order to properly characterize their structural properties.

With the CMD-fitting software package StarFISH, we find the stellar population of Hercules to be old (>12 Gyr) and metal poor ($[Fe/H] \sim -2.0$), albeit with a spread in metallicity. It is interesting to compare the SFH of Hercules both with the other UF satellites and with all satellites that are >100 kpc from the MW. Of the new UF dwarf spheroidals (excluding Leo T, which appears to be a different class of object), only Ursa Major II and Can Ven I have clear, multiple epochs of star formation (de Jong et al. 2008b). That said, formal CMD-fitting has not been performed on data deeper than the SDSS (again excluding Leo T; de Jong et al. 2008a), and so it remains to be seen if many of the new MW satellites harbor small, young populations. Nonetheless, if the current picture of the new satellites holds, Hercules is in the mainstream of these objects, with an old and metal poor population.

The SFH of the classical dSph's as a function of MW distance has long been thought to provide clues as to the relative importance of environmental processes (e.g. ionizing radiation, ram pressure stripping, and supernova feedback) in the galaxy formation process (e.g. van den Bergh 1994). For instance, of the eight classical dwarf spheroidals (excluding the disrupting Sagittarius), the four nearest ($\lesssim$90 kpc) all have primarily ancient stellar populations, while the four furthest all have extended SFHs (for a review of the SFHs of the classical satellites, see Dolphin et al. 2005). Two interpretations are possible when looking at the classical dSph's alone, assuming that the present MW distance of a given satellite is representative of its average MW distance (which is not likely to be the case for all the satellites, e.g. Leo I; Mateo et al. 2008). First, this could signal that environment plays a large role, where tidal and ram pressure stripping of gas or local ionizing radiation serves to truncate SF in the nearest dwarfs. Alternatively, pericentric passages trigger SF, and the nearest systems – which have had more such passages – exhaust their gas quickly (Harris & Zaritsky 2004; Zaritsky & Harris 2004). In this scenario, the new UF satellites would exhibit a similar dichotomy in their SFHs as a function of MW distance as the classical dSphs. The dual nature of the classical dSph's star formation as a function of MW distance could also simply be a function of the size of the initial baryonic reservoir, since the four nearest are also the least luminous. In this instance, the UF satellites would all have primarily ancient stellar populations. While SFHs of the new dwarfs must be derived with deeper data, the presence of multiple epochs of SF in both UMaII (D=30 kpc) and Can Ven I (D=218 kpc), and our result that Hercules (D=133 kpc) has solely an ancient stellar population seems to muddy any picture where either environment or initial baryonic reservoir *solely* determine a satellite's SFH.

As we have mentioned previously, Hercules is a prime candidate for wide-field followup due to its extended morphology and possible hint of kinematic substructure. To investigate this possible kinematic substructure, J. Simon and M. Geha kindly provided their kinematic data on Hercules, which we have overplotted onto our smoothed map of the central field (Figure 15). Red diamonds indicate the location of possible 'substructure' stars – those with velocities between 41 and 43 kms^{-1} – while the blue diamonds are the position of the other stars identified with Hercules. There is no obvious spatial correlation between Hercules structural features and the spatial position of the candidate 'substructure' stars. Further kinematic work will be necessary to confirm any non-Gaussian features in Hercules' velocity histogram.

Can we find a plausible orbit for Hercules that explains its current structure and possible orbital debris? Hercules' great distance (133 kpc), and high velocity away from the MW (145 km s^{-1}) mean that it likely has a fairly elongated orbit. Klessen et al. (2003) explored the consequences of a purely tidal model, with no dark matter and radial orbits, for the dwarf spheroidal galaxy Draco. The hope was that depth along the line of sight in that system would explain Draco's properties. While this model was unsuccessful in that instance, they did show that slight variations in viewing angle along the 'barrel' of a tidal stream could produce the appearance of a highly elongated morphology – similar to that seen in Hercules (see Figure 3 of Klessen et al. 2003). In § 4.2, we searched for and found no evidence for depth along the line of sight, which suggests that a scenario in which we are looking at a tidal stream nearly down its length will have some difficulty explaining Hercules' unusual elongation – although our limit to the line of sight depth of ∼6 kpc is not particularly stringent yet. However, if our tentative evidence that Hercules is embedded in a larger stellar stream seen in the plane of the sky is correct, it is still worth considering that Hercules had a significant encounter with the MW at perigalacticon.

As an exercise, we calculated a series of orbits for a point-like Hercules model in a static, multicomponent Galactic potential identical to Johnston et al. (1995) with reasonable assumed values of the tangential velocity along both the minor and major axis of Hercules. The resulting orbits can then be compared with the observed orbital properties of the other MW satellites. We explore eight different cases, with four having a proper motion vector in the Galactic Rest Frame (GRF) along Hercules' major axis and to the East (cases 1-4), while four have GRF tangential motion along Hercules' minor axis and to the North. Orbital elements for our eight principal cases are presented in Table 6. Cases 1 through 4 all exhibit roughly polar orbits, a common feature among the MW satellites (e.g. Palma et al. 2002). The pericentric radius of cases 1 and 2 make it unlikely that Hercules would have survived as a bound object over a Hubble time, while case 3 would likely have also caused damage (see e.g. Mayer et al. 2001; Mateo 2008). Case 4 would probably allow for Hercules to survive a

Hubble time. If case 3 is close to Hercules' true orbit, then it would lie near the orbital pole grouping of some of the other dwarf spheroidals claimed by Kroupa et al. (2005). In cases 5 through 8, where the GRF tangential motion is along Hercules' minor axis and to the North, the inclination approaches the equatorial case. Only case 8 would allow long-term survival of Hercules. These models are all speculative at this point, but if Hercules has similar orbital properties as the other MW satellites, we would expect future proper motion measurements to be nearest our case 3, due to the polar orbit, the orbital pole in the vicinity of the other satellites, and an intermediate perigalacticon distance. With the refurbishment of HST and the installation of WF3, it will be possible to measure the proper motion of Hercules and derive its orbit, which will be critical for understanding the true nature of this object.

There is more wide-field imaging work to be done on Hercules. It would be worth obtaining more complete sky coverage in its vicinity, and to go to greater depth. For instance, our western pointings were not optimally placed to search for external structure in that direction and deeper data in our eastern fields (comparable to that obtained in our central pointing) would shed light on whether or not the eastern nuggets are truly remnants of Hercules. Data to fill in regions to the north and south of Hercules would also be of interest.

While the nature of Hercules remains elusive, we now have the tools in place to study all of the new MW satellites in detail. There is a critical need for more in depth study of all of the new MW satellites to understand their structure, star formation history and dynamical state – and to ultimately put them into context with respect to the Cold Dark Matter paradigm for structure formation.

REFERENCES

Adelman-McCarthy, J. K., Agüeros, M. A., Allam, S. S., Anderson, K. S. J., Anderson, S. F., Annis, J., Bahcall, N. A., Baldry, I. K., Barentine, J. C., Berlind, A., Bernardi, M., Blanton, M. R., Boroski, W. N., Brewington, H. J., Brinchmann, J., Brinkmann, J.,

Brunner, R. J., Budavári, T., Carey, L. N., Carr, M. A., Castander, F. J., Connolly, A. J., Csabai, I., Czarapata, P. C., Dalcanton, J. J., Doi, M., Dong, F., Eisenstein, D. J., Evans, M. L., Fan, X., Finkbeiner, D. P., Friedman, S. D., Frieman, J. A., Fukugita, M., Gillespie, B., Glazebrook, K., Gray, J., Grebel, E. K., Gunn, J. E., Gurbani, V. K., de Haas, E., Hall, P. B., Harris, F. H., Harvanek, M., Hawley, S. L., Hayes, J., Hendry, J. S., Hennessy, G. S., Hindsley, R. B., Hirata, C. M., Hogan, C. J., Hogg, D. W., Holmgren, D. J., Holtzman, J. A., Ichikawa, S.-i., Ivezić, Ž., Jester, S., Johnston, D. E., Jorgensen, A. M., Jurić, M., Kent, S. M., Kleinman, S. J., Knapp, G. R., Kniazev, A. Y., Kron, R. G., Krzesinski, J., Kuropatkin, N., Lamb, D. Q., Lampeitl, H., Lee, B. C., Leger, R. F., Lin, H., Long, D. C., Loveday, J., Lupton, R. H., Margon, B., Martínez-Delgado, D., Mandelbaum, R., Matsubara, T., McGehee, P. M., McKay, T. A., Meiksin, A., Munn, J. A., Nakajima, R., Nash, T., Neilsen, Jr., E. H., Newberg, H. J., Newman, P. R., Nichol, R. C., Nicinski, T., Nieto-Santisteban, M., Nitta, A., O'Mullane, W., Okamura, S., Owen, R., Padmanabhan, N., Pauls, G., Peoples, J. J., Pier, J. R., Pope, A. C., Pourbaix, D., Quinn, T. R., Richards, G. T., Richmond, M. W., Rockosi, C. M., Schlegel, D. J., Schneider, D. P., Schroeder, J., Scranton, R., Seljak, U., Sheldon, E., Shimasaku, K., Smith, J. A., Smolčić, V., Snedden, S. A., Stoughton, C., Strauss, M. A., SubbaRao, M., Szalay, A. S., Szapudi, I., Szkody, P., Tegmark, M., Thakar, A. R., Tucker, D. L., Uomoto, A., Vanden Berk, D. E., Vandenberg, J., Vogeley, M. S., Voges, W., Vogt, N. P., Walkowicz, L. M., Weinberg, D. H., West, A. A., White, S. D. M., Xu, Y., Yanny, B., Yocum, D. R., York, D. G., Zehavi, I., Zibetti, S., & Zucker, D. B. 2006, ApJS, 162, 38

Belokurov, V., Walker, M. G., Evans, N. W., Faria, D. C., Gilmore, G., Irwin, M. J., Koposov, S., Mateo, M., Olszewski, E., & Zucker, D. B. 2008, ApJ, 686, L83

Belokurov, V., Zucker, D. B., Evans, N. W., Gilmore, G., Vidrih, S., Bramich, D. M., Newberg, H. J., Wyse, R. F. G., Irwin, M. J., Fellhauer, M., Hewett, P. C., Walton, N. A., Wilkinson, M. I., Cole, N., Yanny, B., Rockosi, C. M., Beers, T. C., Bell, E. F., Brinkmann, J., Ivezić, Ž., & Lupton, R. 2006, ApJ, 642, L137

Belokurov, V., Zucker, D. B., Evans, N. W., Kleyna, J. T., Koposov, S., Hodgkin, S. T., Irwin, M. J., Gilmore, G., Wilkinson, M. I., Fellhauer, M., Bramich, D. M., Hewett, P. C., Vidrih, S., De Jong, J. T. A., Smith, J. A., Rix, H.-W., Bell, E. F., Wyse, R. F. G., Newberg, H. J., Mayeur, P. A., Yanny, B., Rockosi, C. M., Gnedin, O. Y., Schneider, D. P., Beers, T. C., Barentine, J. C., Brewington, H., Brinkmann, J., Harvanek, M., Kleinman, S. J., Krzesinski, J., Long, D., Nitta, A., & Snedden, S. A. 2007, ApJ, 654, 897

Bertin, E. 2006, in Astronomical Society of the Pacific Conference Series, Vol. 351, Astronomical Data Analysis Software and Systems XV, ed. C. Gabriel, C. Arviset, D. Ponz, & S. Enrique, 112–+

Bullock, J. S. & Johnston, K. V. 2005, ApJ, 635, 931

Cho, D.-H., Lee, S.-G., Jeon, Y.-B., & Sim, K. J. 2005, AJ, 129, 1922

Clem, J. L., Vanden Berg, D. A., & Stetson, P. B. 2008, AJ, 135, 682

Coleman, M. G., Da Costa, G. S., Bland-Hawthorn, J., & Freeman, K. C. 2005, AJ, 129, 1443

Coleman, M. G., de Jong, J. T. A., Martin, N. F., Rix, H.-W., Sand, D. J., Bell, E. F., Pogge, R. W., Thompson, D. J., Hippelein, H., Giallongo, E., Ragazzoni, R., DiPaola, A., Farinato, J., Smareglia, R., Testa, V., Bechtold, J., Hill, J. M., Garnavich, P. M., & Green, R. F. 2007, ApJ, 668, L43

de Jong, J. T. A., Harris, J., Coleman, M. G., Martin, N. F., Bell, E. F., Rix, H.-W., Hill, J. M., Skillman, E. D., Sand, D. J., Olszewski, E. W., Zaritsky, D., Thompson, D., Giallongo, E., Ragazzoni, R., DiPaola, A., Farinato, J., Testa, V., & Bechtold, J. 2008a, ApJ, 680, 1112

de Jong, J. T. A., Rix, H.-W., Martin, N. F., Zucker, D. B., Dolphin, A. E., Bell, E. F., Belokurov, V., & Evans, N. W. 2008b, AJ, 135, 1361

Dolphin, A. E. 2002, MNRAS, 332, 91

Dolphin, A. E., Weisz, D. R., Skillman, E. D., & Holtzman, J. A. 2005, ArXiv Astrophysics e-prints

Dotter, A., Chaboyer, B., Jevremović, D., Kostov, V., Baron, E., & Ferguson, J. W. 2008, ApJS, 178, 89

Geha, M., Willman, B., Simon, J. D., Strigari, L. E., Kirby, E. N., Law, D. R., & Strader, J. 2009, ApJ, 692, 1464

Girardi, L., Bertelli, G., Bressan, A., Chiosi, C., Groenewegen, M. A. T., Marigo, P., Salasnich, B., & Weiss, A. 2002, A&A, 391, 195

Girardi, L., Grebel, E. K., Odenkirchen, M., & Chiosi, C. 2004, A&A, 422, 205

Grillmair, C. J. 2009, ApJ, 693, 1118

Grundahl, F., Stetson, P. B., & Andersen, M. I. 2002, A&A, 395, 481

Harris, J. 2007, ApJ, 658, 345

Harris, J. & Zaritsky, D. 2001, ApJS, 136, 25

—. 2004, AJ, 127, 1531

Ibata, R. A., Gilmore, G., & Irwin, M. J. 1994, Nature, 370, 194

Johnston, K. V., Spergel, D. N., & Hernquist, L. 1995, ApJ, 451, 598

Jordi, K., Grebel, E. K., & Ammon, K. 2006, A&A, 460, 339

King, I. R. 1966, AJ, 71, 64

Kirby, E. N., Simon, J. D., Geha, M., Guhathakurta, P., & Frebel, A. 2008, ApJ, 685, L43

Klessen, R. S., Grebel, E. K., & Harbeck, D. 2003, ApJ, 589, 798

Koch, A., McWilliam, A., Grebel, E. K., Zucker, D. B., & Belokurov, V. 2008, ApJ, 688, L13

Kraft, R. P. & Ivans, I. I. 2003, PASP, 115, 143

Kravtsov, A. V., Gnedin, O. Y., & Klypin, A. A. 2004, ApJ, 609, 482

Kroupa, P., Theis, C., & Boily, C. M. 2005, A&A, 431, 517

Martin, N. F., Coleman, M. G., De Jong, J. T. A., Rix, H.-W., Bell, E. F., Sand, D. J., Hill, J. M., Thompson, D., Burwitz, V., Giallongo, E., Ragazzoni, R., Diolaiti, E., Gasparo, F., Grazian, A., Pedichini, F., & Bechtold, J. 2008a, ApJ, 672, L13

Martin, N. F., de Jong, J. T. A., & Rix, H.-W. 2008b, ApJ, 684, 1075

Mateo, M. 2008, The Complex Evolution of Simple Systems

Mateo, M., Olszewski, E. W., & Walker, M. G. 2008, ApJ, 675, 201

Mayer, L., Governato, F., Colpi, M., Moore, B., Quinn, T., Wadsley, J., Stadel, J., & Lake, G. 2001, ApJ, 559, 754

Muñoz, R. R., Carlin, J. L., Frinchaboy, P. M., Nidever, D. L., Majewski, S. R., & Patterson, R. J. 2006, ApJ, 650, L51

Odenkirchen, M., Grebel, E. K., Dehnen, W., Rix, H.-W., Yanny, B., Newberg, H. J., Rockosi, C. M., Martínez-Delgado, D., Brinkmann, J., & Pier, J. R. 2003, AJ, 126, 2385

Okamoto, S., Arimoto, N., Yamada, Y., & Onodera, M. 2008, A&A, 487, 103

Palma, C., Majewski, S. R., & Johnston, K. V. 2002, ApJ, 564, 736

Paust, N. E. Q., Chaboyer, B., & Sarajedini, A. 2007, AJ, 133, 2787

Plummer, H. C. 1911, MNRAS, 71, 460

Press, W. H., Flannery, B. P., Teukolsky, S. A., & Vetterling, W. T. 1988, Numerical recipes in C: the art of scientific computing (New York, NY, USA: Cambridge University Press)

Ragazzoni, R., Giallongo, E., Pasian, F., Baruffolo, A., Bertram, R., Diolaiti, E., Di Paola, A., Farinato, J., Gentile, G., Hill, J., Lombini, M., Pedichini, F., Speziali, R., Smareglia, R., & Vernet, E. 2006, in Presented at the Society of Photo-Optical Instrumentation Engineers (SPIE) Conference, Vol. 6267, Ground-based and Airborne Telescopes. Edited by Stepp, Larry M.. Proceedings of the SPIE, Volume 6267, pp. 626710 (2006).

Rider, C. J., Tucker, D. L., Smith, J. A., Stoughton, C., Allam, S. S., & Neilsen, Jr., E. H. 2004, AJ, 127, 2210

Schlegel, D. J., Finkbeiner, D. P., & Davis, M. 1998, ApJ, 500, 525

Simon, J. D. & Geha, M. 2007, ApJ, 670, 313

Stetson, P. B. 1994, PASP, 106, 250

Strigari, L. E., Bullock, J. S., Kaplinghat, M., Simon, J. D., Geha, M., Willman, B., & Walker, M. G. 2008, Nature, 454, 1096

van den Bergh, S. 1994, ApJ, 428, 617

van Dokkum, P. G. 2001, PASP, 113, 1420

Walker, M. G., Mateo, M., Olszewski, E. W., Peñarrubia, J., Wyn Evans, N., & Gilmore, G. 2009, ArXiv e-prints

Walsh, S. M., Willman, B., Sand, D., Harris, J., Seth, A., Zaritsky, D., & Jerjen, H. 2008, ApJ, 688, 245

Willman, B., Masjedi, M., Hogg, D. W., Dalcanton, J. J., Martinez-Delgado, D., Blanton, M., West, A. A., Dotter, A., & Chaboyer, B. 2006, ArXiv Astrophysics e-prints

Zaritsky, D. & Harris, J. 2004, ApJ, 604, 167

Zucker, D. B., Belokurov, V., Evans, N. W., Kleyna, J. T., Irwin, M. J., Wilkinson, M. I., Fellhauer, M., Bramich, D. M., Gilmore, G., Newberg, H. J., Yanny, B., Smith, J. A., Hewett, P. C., Bell, E. F., Rix, H.-W., Gnedin, O. Y., Vidrih, S., Wyse, R. F. G., Willman, B., Grebel, E. K., Schneider, D. P., Beers, T. C., Kniazev, A. Y., Barentine, J. C., Brewington, H., Brinkmann, J., Harvanek, M., Kleinman, S. J., Krzesinski, J., Long, D., Nitta, A., & Snedden, S. A. 2006, ApJ, 650, L41
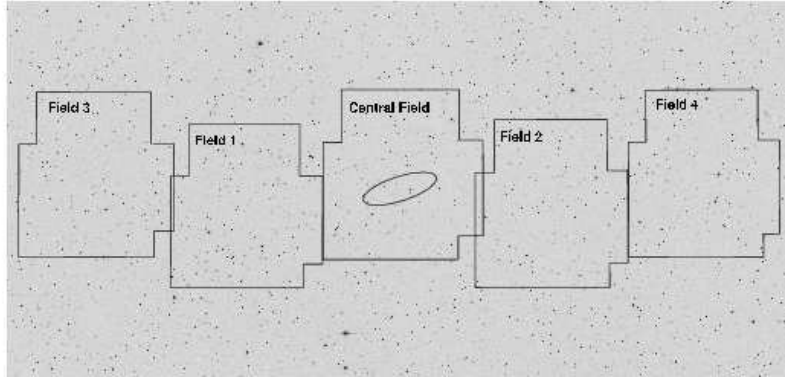
Fig. 1.— An outline of our five LBT pointings on a Digital Sky Survey image backdrop. The ellipse in the central pointing shows the orientation and half light radius of Hercules, as determined for an exponential profile in § 3.2. For a sense of scale, each LBT pointing is roughly 23' along its base. North is up and East is to the left.
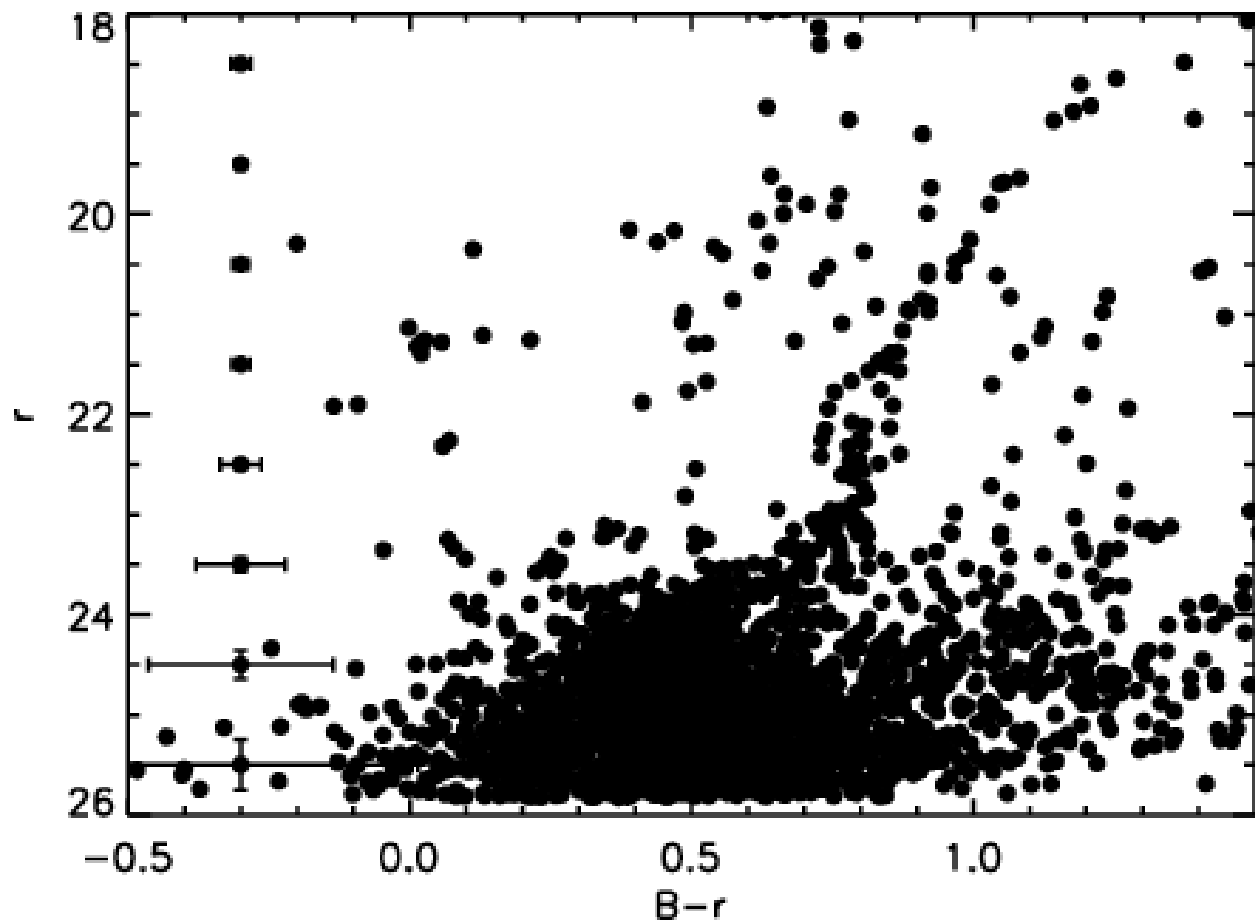
Fig. 2.— $B - r$ versus r color magnitude diagram of stars within a 5.9' elliptical radius (the exponential profile half light radius) of the center of Hercules. Error bars showing the color and magitude uncertainties as a function of r are overplotted.
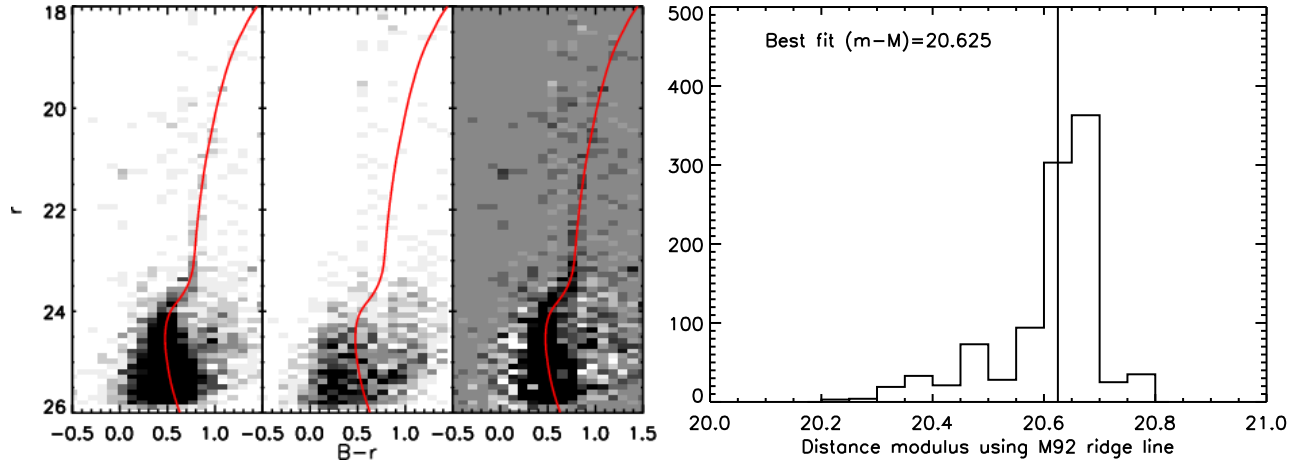
Fig. 3.— Results of our empirical determination of Hercules' distance modulus using an M92 fiducial. **Left** – A three-panel Hess diagram of the region within one half light radius of Hercules. The left panel shows all stars within this radius, the center panel shows an equivalent area background Hess diagram while the right panel shows the background subtracted Hess diagram of Hercules. Overplotted in red in all three panels is an M92 fiducial transformed to a distance modulus of 20.625. **Right** – Histogram results of our bootstrap resampling error analysis for the distance modulus of Hercules. Eighty percent of the bootstrap resamples are within $(m - M)$=20.625 $\pm$ 0.1 and so we adopt this as our conservative uncertainty on the measurement.
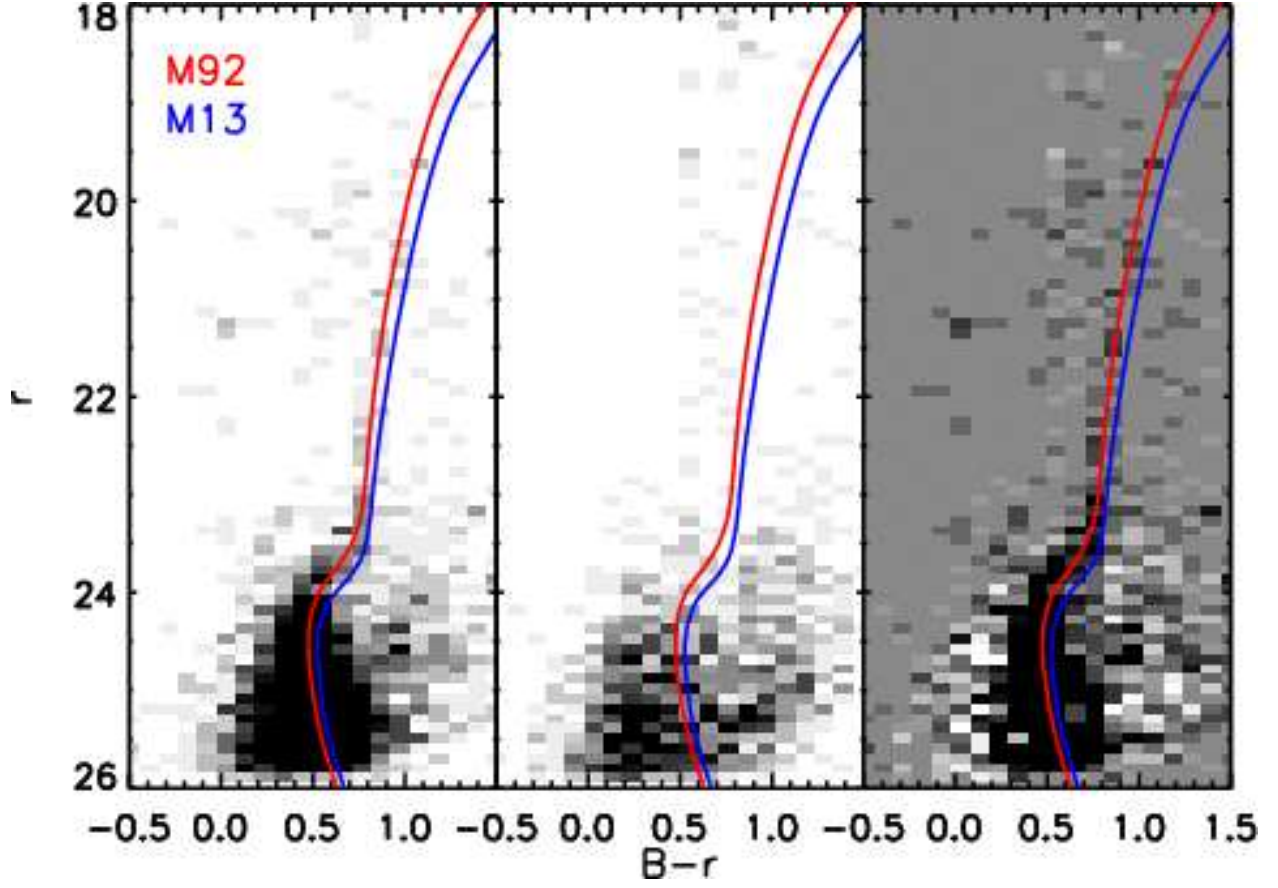
Fig. 4.— Hess diagram with both M92 ($[Fe/H] = -2.4$;red) and M13 ($[Fe/H] = -1.57$;blue) at a distance modulus of 20.625. While the M92 isochrone produces the best match to Hercules' CMD, there may be lower metallicity components to its stellar population. Given the zeropoint uncertainties of $\delta r \sim 0.03$ and $\delta B \sim 0.05$, our CMDs are also consistent with a more moderate metal abundance.
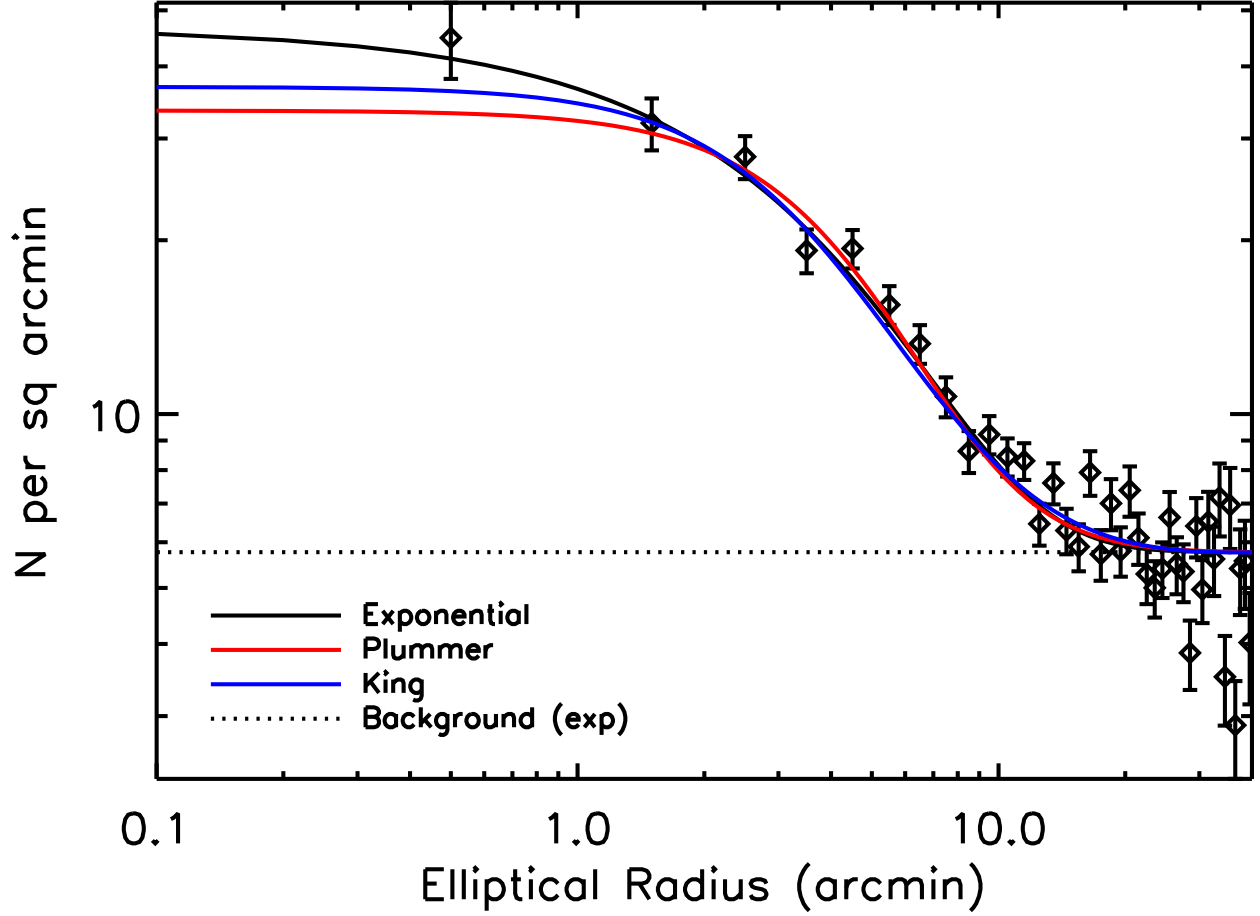
Fig. 5.— Stellar profile of Hercules. The data points are the binned star counts for all stars in our central pointing which are consistent with the $(m - M)$=20.625 M92 fiducial. The plotted lines show the best fit one-dimensional exponential, Plummer and King profiles. Note that in deriving these best fits, we are not fitting to the binned data, but directly to the stellar distribution.
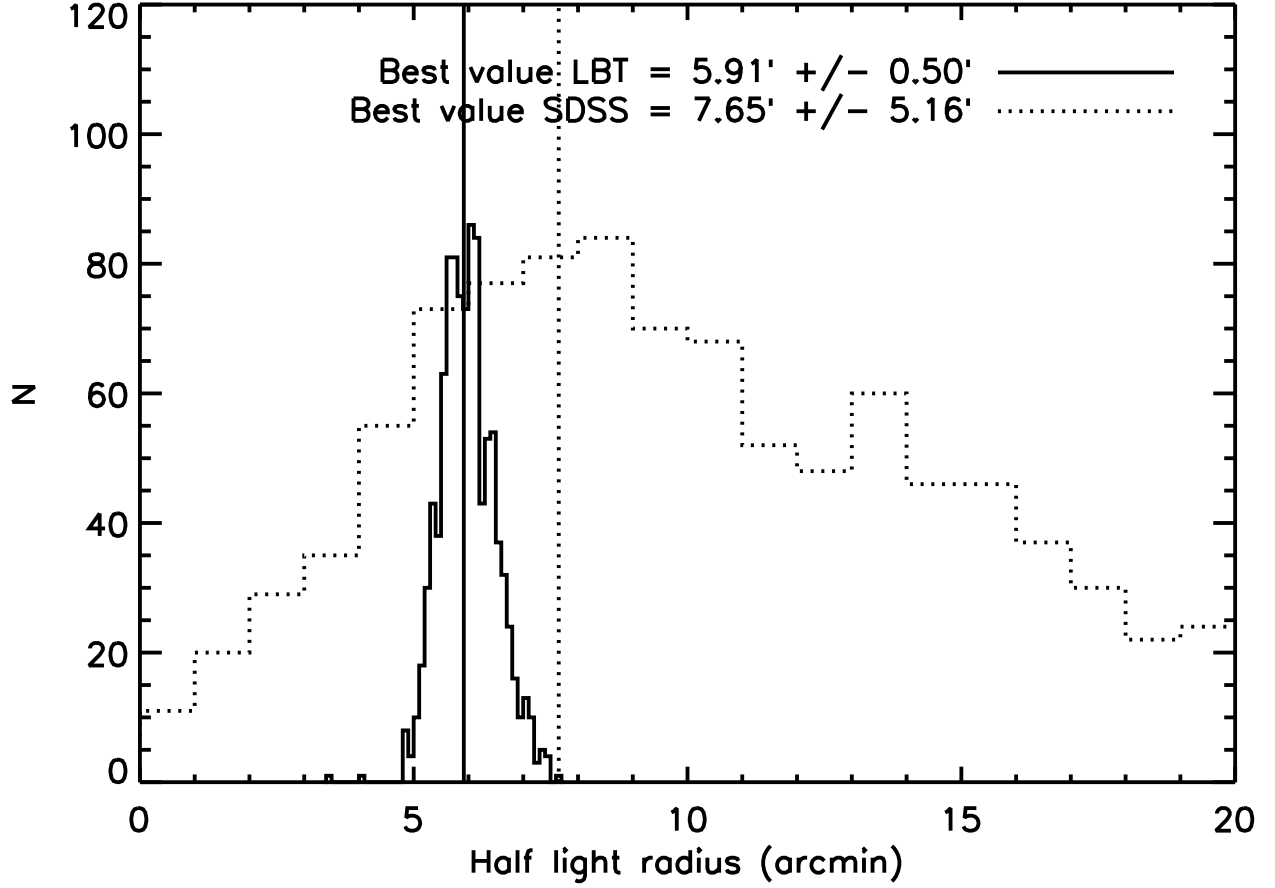
Fig. 6.— Histogram showing the results of our bootstrap resampling when measuring r_h, using both the LBT data and that taken from SDSS. While the SDSS and LBT data are generally in good agreement within the uncertainties, this clearly illustrates the need for deep data for the new MW satellites.
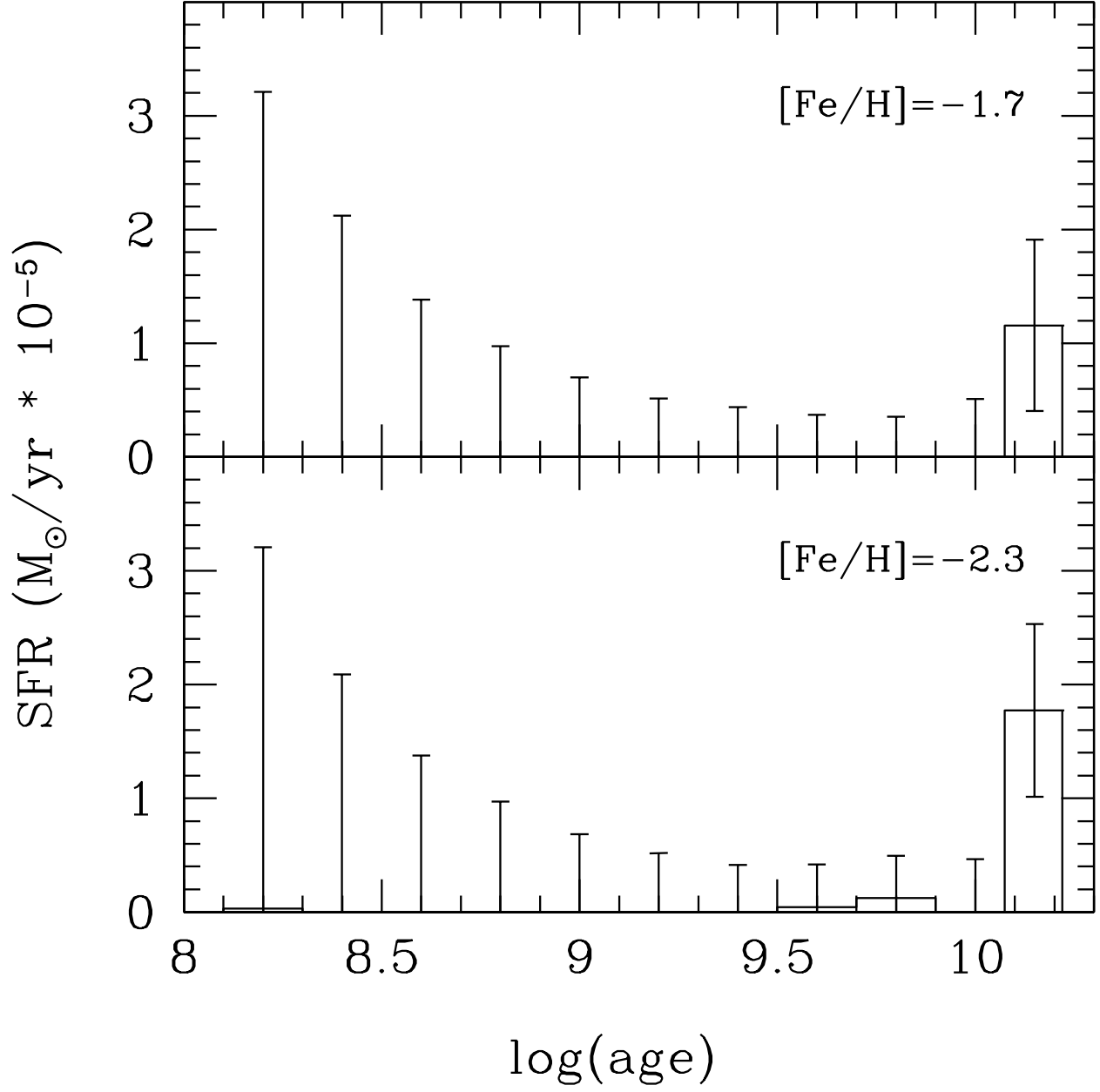
Fig. 7.— SFH solution from the StarFISH fit. Only the [Fe/H]=−2.3 and −1.7 bins contributed to the solution and so are the only ones plotted here. Hercules consists of an old metal poor population, with some indication of metallicity spread. Error bars with no accompanying histogram are upper limits.
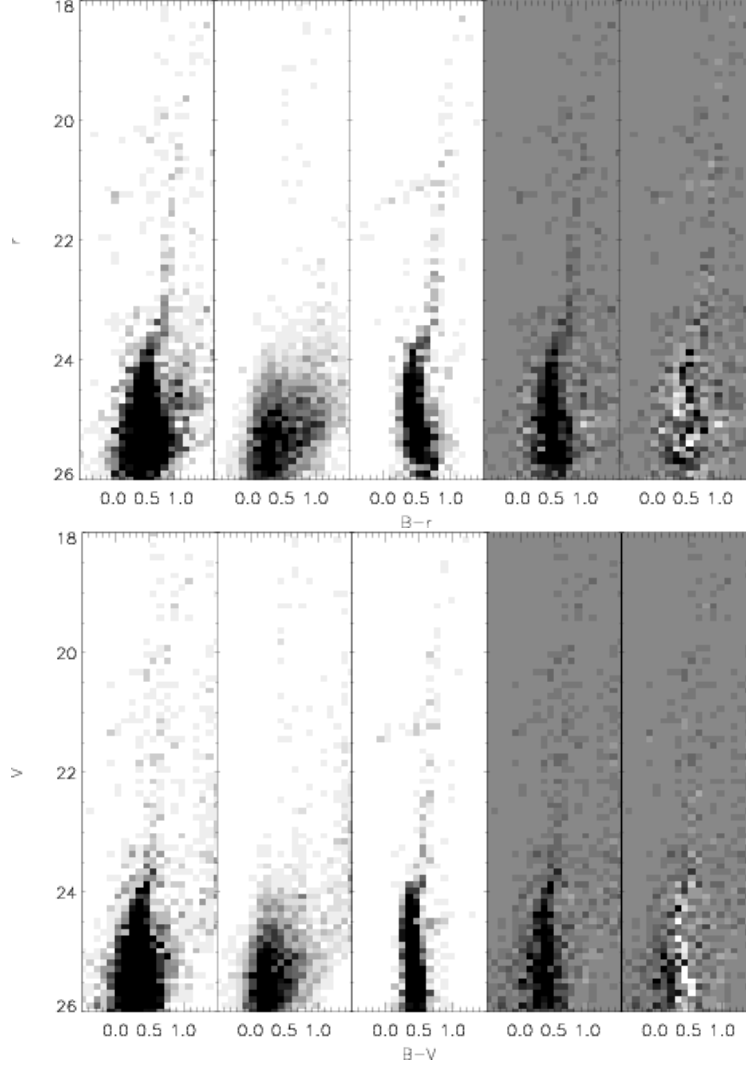
Fig. 8.— Comparison of data to best StarFISH model fit. The top panel is for our $B - r$ versus r data, and the bottom for $B - V$ versus V. **Left**– Raw Hess diagram of the central r_h =5.9' of Hercules. **Second Left** – Background Hess diagram. **Center** – The Hess diagram of the synthetic populations corresponding to the best-fit StarFISH solution. **Second Right** – Background subtracted Hess diagram of the central r_h =5.9' of Hercules. **Far Right** – Residual Hess diagram after subtraction of the best-fit StarFISH model from the background subtracted data.
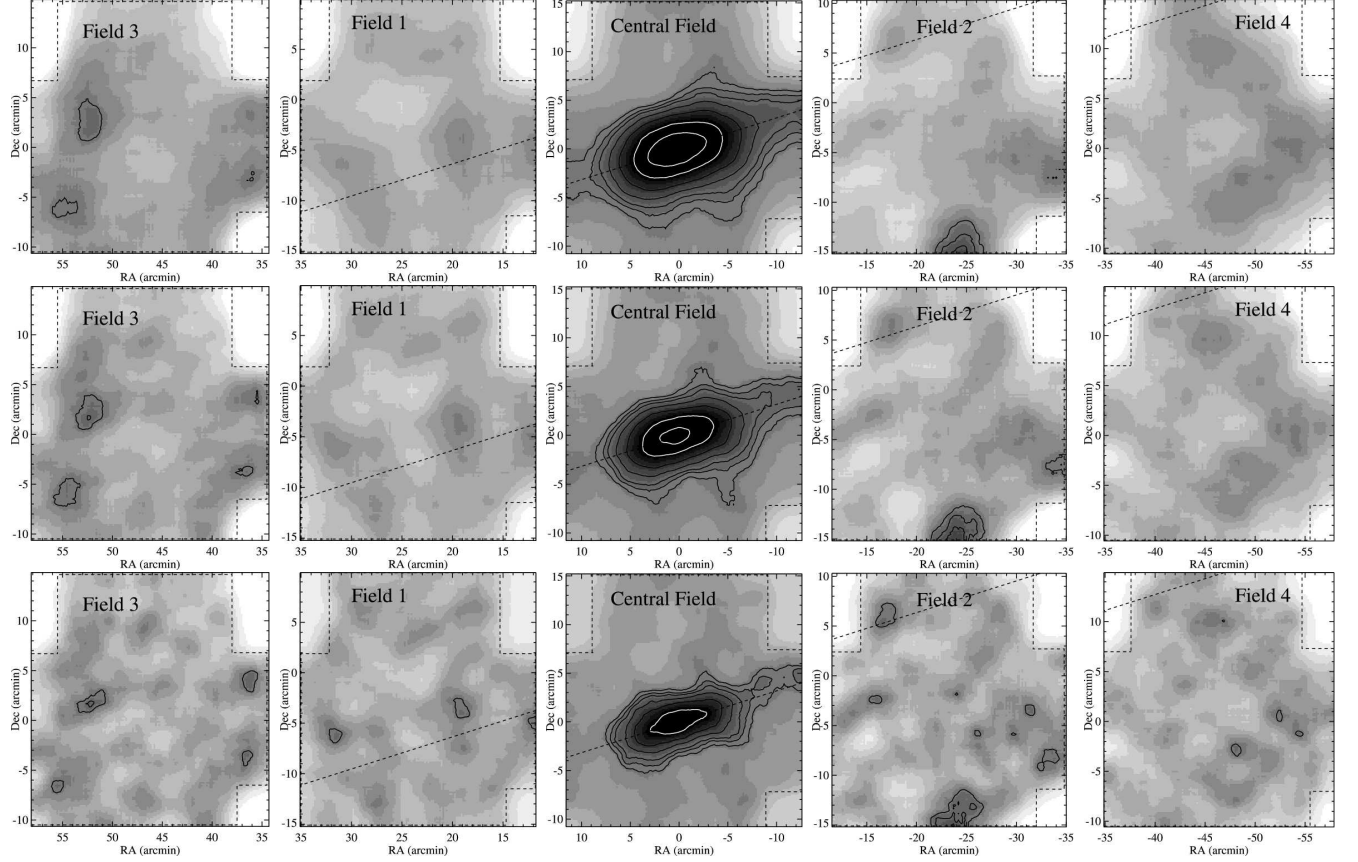
Fig. 9.— Smoothed contour plots of Hercules and adjacent fields. The contours show the 3, 4, 5, 7, 10, 15 and 20 σ levels. Each row shows our Hercules pointings arranged from East to West, with the middle panel roughly centered on the position of Hercules. The top row shows contour plots after smoothing the data by 2 arcmin. The middle row is smoothed by 1.5 arcmin, and the bottom row is smoothed by 1 arcmin. Dashed lines represent the actual LBT field of view. The dashed line going through the center of Hercules traces the position angle found for our exponential profile fit presented in § 3.2, $\theta = -72.4$ degrees.
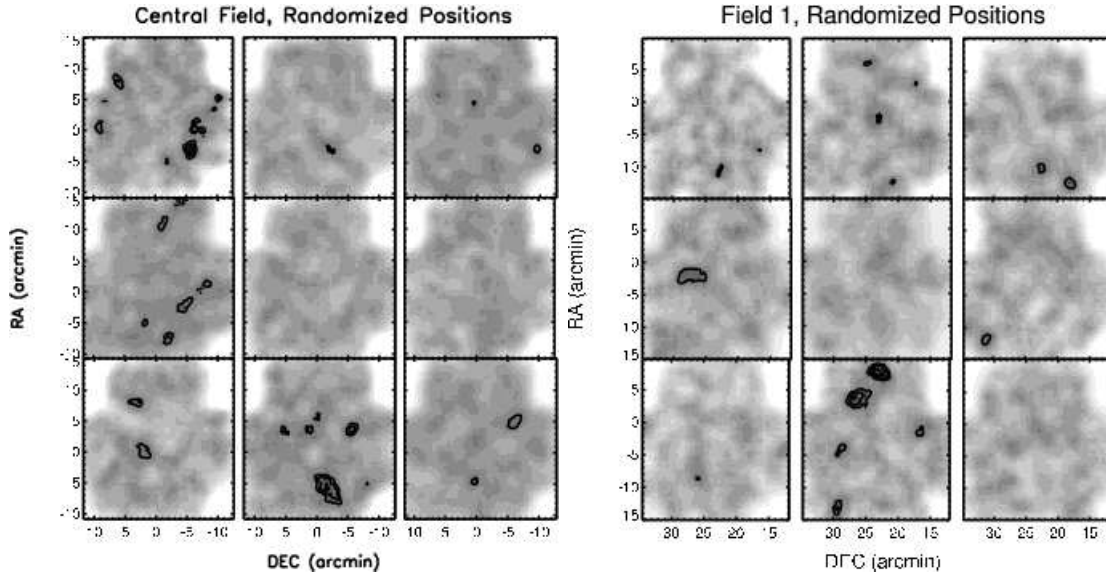
Fig. 10.— Smoothed contour plots, made as in Fig 9, of nine random realizations of Hercules stars where we have reassigned star positions with ones drawn from a uniform distribution across the LBT field of view. The left panel shows results from our central Hercules pointing photometry, while the right panel shows results using our Field 1 photometry. The contours show the 3, 4, and 5 σ levels. The plots show that 3σ overdensities are relatively common.
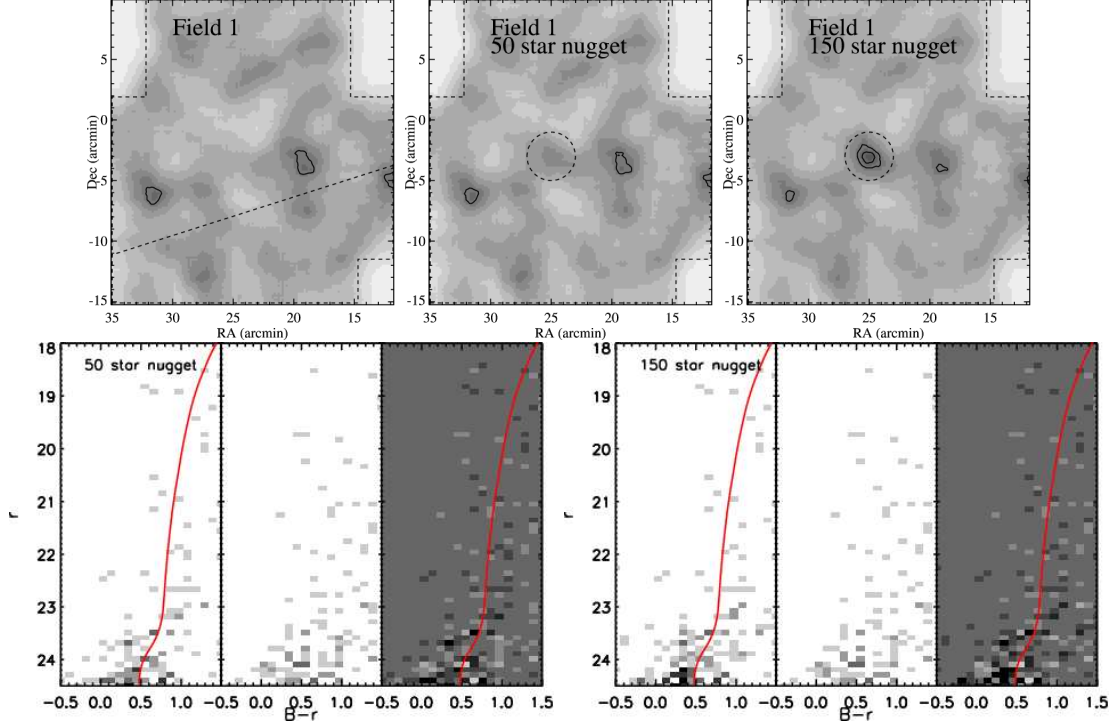
Fig. 11.— An illustration of our technique for implanting fake Hercules 'nuggets' into our fields. Each of these 'nuggets' has the same SFH as Hercules, taking into account the results of our artificial star tests in this field. On the top row, from left to right, we show first Field 1 smoothed with a $\sigma = 1$ arcminute Gaussian. In the center and right panel we show this same field after injecting 'nuggets' with 50 and 150 stars, respectively, distributed as an exponential with a half light radius of 3 arcminutes (see Table 5). These nuggets are similar in size as the real stellar overdensities in the field. Bottom – Hess diagrams of the two nuggets inserted into the image shown in the top row, along with the M92 isochrone shifted to $(m - M) = 20.625$. These Hess diagrams are made identically to those in § 4.1.2, with an equal area annulus outside the encircled region serving as the background CMD. Note that, despite the high significance of the 150 star nugget it is difficult to say for certain that the CMD is similar to Hercules, although there is an indication of the beginning of a main sequence around $r \sim 24.2$. It is difficult to see such a feature in the 50 star nugget's background-subtracted Hess diagram.
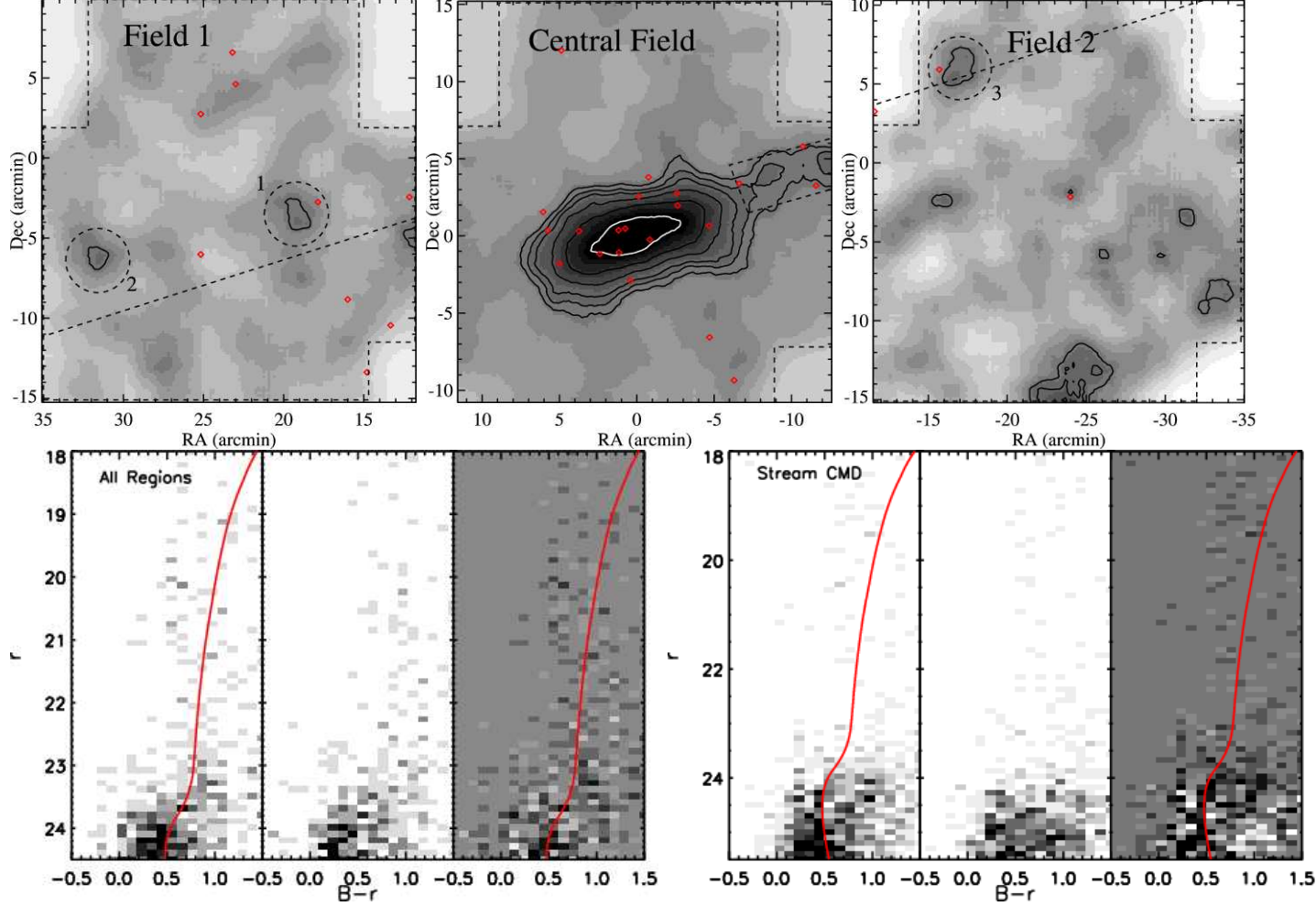
Fig. 12.— Top Row – Smoothed maps of Hercules and Fields 1 and 2, highlighting possible external structure associated with Hercules. The marked regions are used to make the two Hess diagrams shown in the bottom row. Candidate Hercules BHB stars are shown as red diamonds. Bottom row – Hess diagrams of the stream region in the central pointing (Right) and the three nuggets projected nearly along the major axis of Hercules (Left). Both Hess diagrams have features that are consistent with being Hercules stars, although the results should be considered tentative given our randomized tests presented in § 4.1.
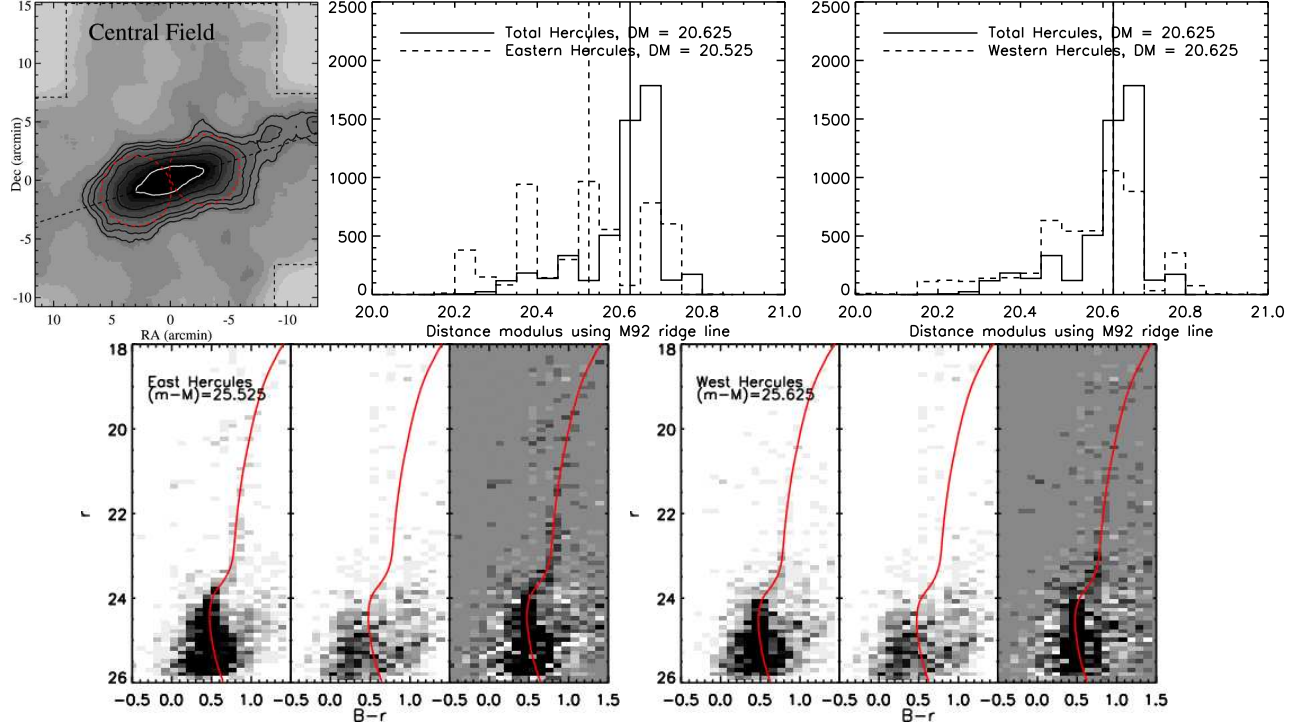
Fig. 13.— Upper Left – An illustration of the two regions in which we separately measured the distance modulus, as in § 3.1, which roughly covers the central half light radius (5.9 arcmin). Upper center and right – Bootstrap histograms of the distance modulus for the eastern and western portions of Hercules, in comparison to that of Hercules as a whole. Note that the Eastern portions seems to be closer (127 kpc) and has a very different histogram in comparison to Hercules as a whole and its western portion. Bottom left and right – Hess diagrams of the East and West portions of Hercules, along with the best-fitting M92 isochrone transformed to the appropriate distance modulus.
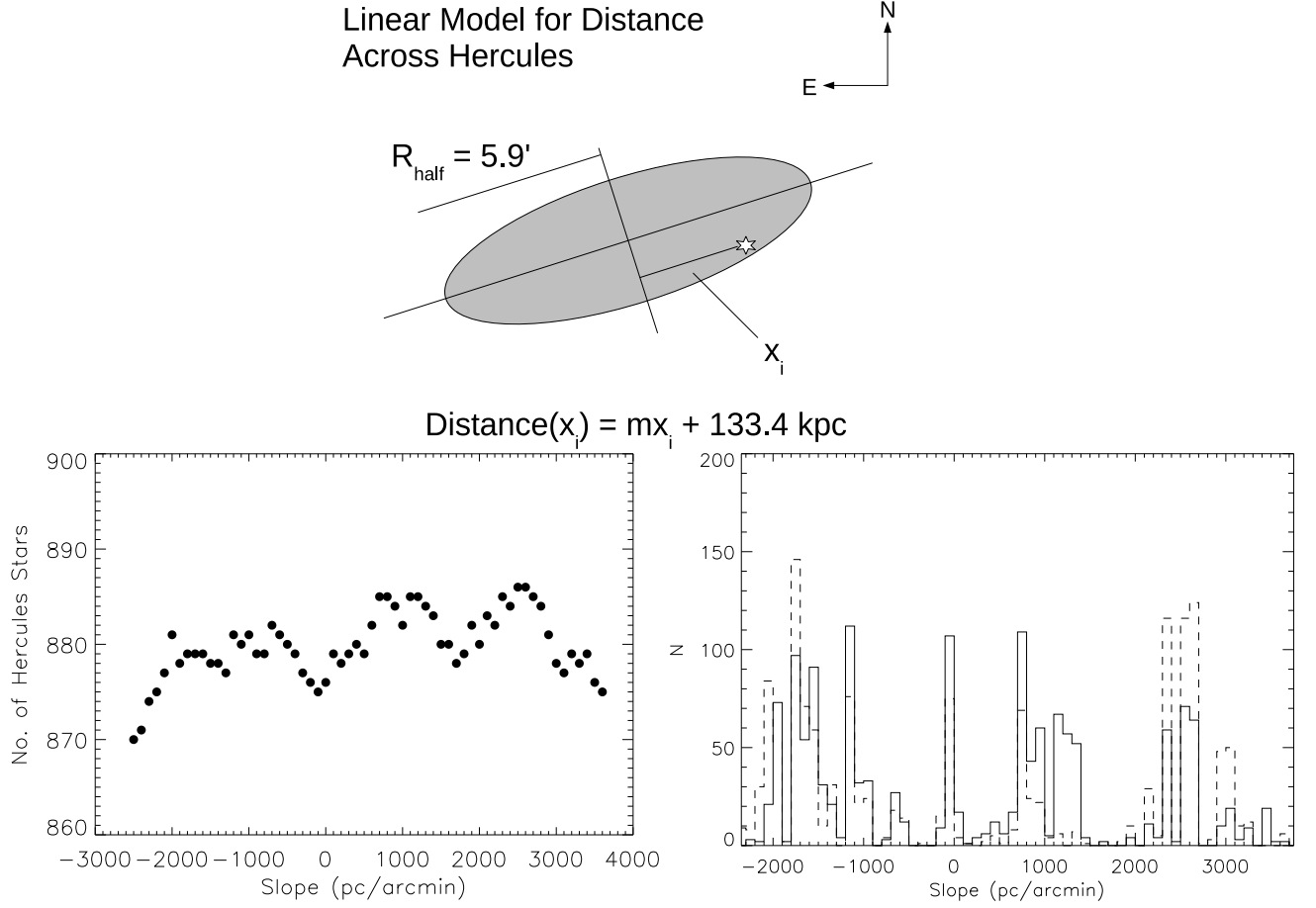
Fig. 14.— Top – A cartoon illustrating our model for the observer-Hercules distance changing as a function of major axis distance. Bottom Left – The number of Hercules stars, after background subtraction, as a function of slope, m. Bottom Right – Histogram of the best-fitting slope with 1500 bootstrap resamples in which we fit our linearly changing distance model. The solid histogram corrsponds to the best-fitting slope that maximized the number of Hercules stars for each of our bootstrap resamples, while the dashed line indicates which slope corresponded to the minimum number of background stars. There is no dominant, preferred slope and the best-fitting slope very often corresponds to a minimum in the background, rather than a maximum in the Hercules-centered ellipse.
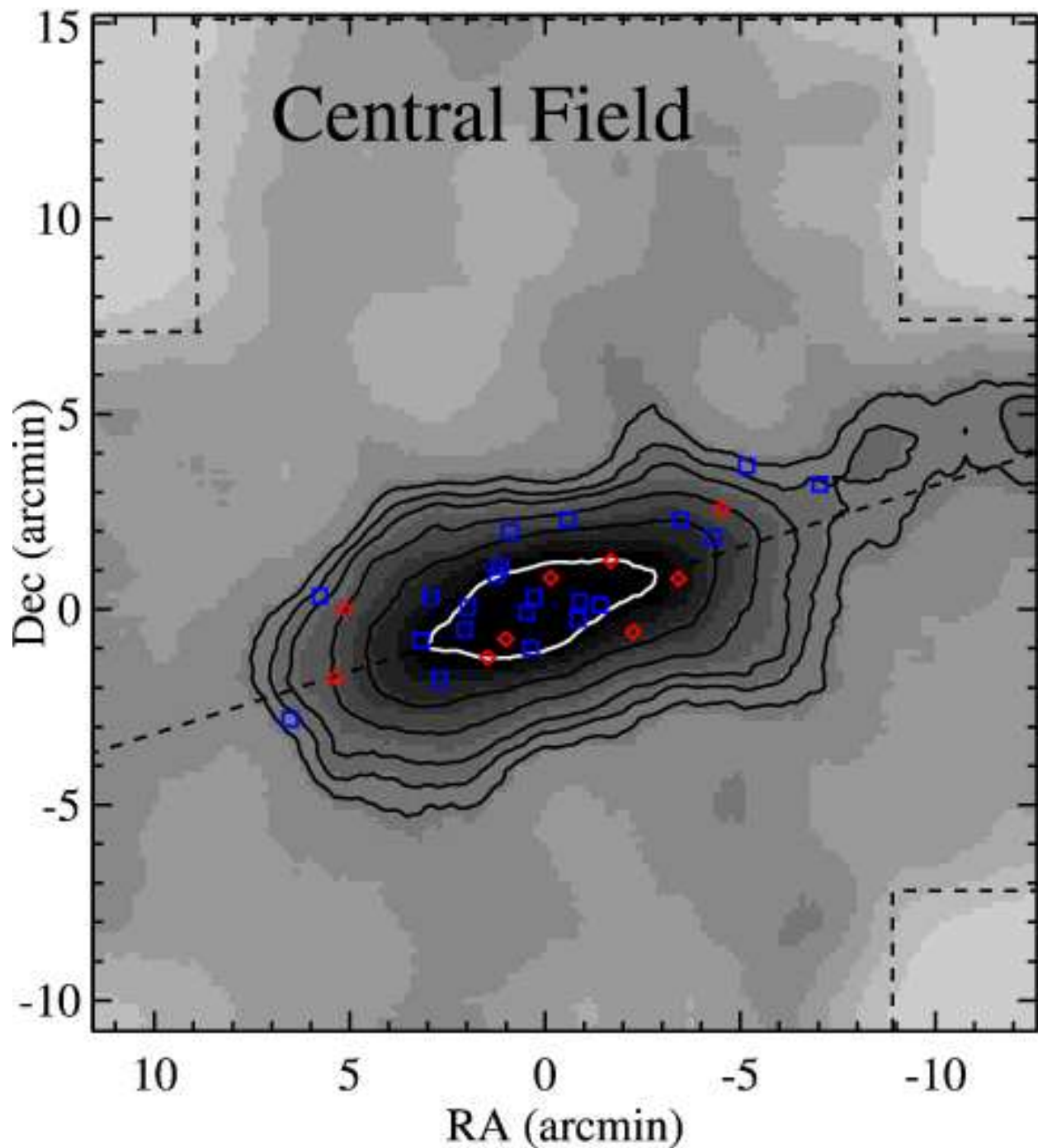
Fig. 15.— The positions of stars with kinematic measurements overplotted onto the smoothed map of Hercules. The red diamonds coincide with the possible 'substructure' stars identified by Simon & Geha (2007) between 41 and 43 kms^{-1}, while the blue boxes represent the other Hercules members with velocities. There is no indication of spatial segregation of the kinematically interesting points, and nor do they coincide with any particular features in Hercules.

Table 1.   Summary of LBT observations and completeness by field

Pointing	UT Date	α (J2000.0)	δ (J2000.0)	Filter	Exposure Time (sec)	Seeing [a] (arcsec)	50% Comp. (mag)	90% Comp. (mag)	95% Comp. (m
Central	2007 Mar 17	16:31:01.99	+12:47:30.12	B	5×300	0.8	26.1	23.9	21.6
	2007 Mar 17			V	4×300	1.0	26.0	24.2	21.8
	2008 June 1			r	5×300	0.9	25.4	23.5	21.1
1	2008 May 29	16:32:37.44	+12:43:11.28	B	6×300	1.3	25.2	23.0	21.6
	2008 May 29			r	5×300	0.9	24.6	22.5	21.0
2	2008 May 30	16:29:26.64	+12:43:11.10	B	6×300	1.4	25.2	23.9	22.0
	2008 May 30			r	5×300	0.9	24.6	22.9	21.8
3	2008 June 2-3	16:34:12.719	+12:47:30.84	B	6×300	1.2	25.0	23.4	21.4
	2008 May 30			r	6×300	1.1	24.5	23.1	20.9
4	2008 June 03, May 31	16:27:51.36	+12:47:30.98	B	5×300	1.2	25.1	23.0	21.7
	2008 May 31			r	5×300	0.9	24.6	22.6	21.2

[a]Seeing value is that of the center of the field of the combined frame.

Table 2.   Hercules Photometry – Central Field

Star No.	α (deg J2000.0)	δ (deg J2000.0)	B (mag)	δB (mag)	A_B (mag)	V (mag)	δV (mag)	A_V (mag)	r (mag)	δr (mag)	A_r (mag)	SDSS or LBT
0	247.74718	12.79046	20.16	0.02	0.26	19.17	0.02	0.20	18.81	0.01	0.17	SDSS
1	247.74373	12.78842	18.88	0.01	0.26	18.28	0.01	0.20	18.12	0.01	0.17	SDSS
2	247.74659	12.80174	18.87	0.01	0.26	18.30	0.01	0.20	18.14	0.01	0.16	SDSS
3	247.74539	12.78312	18.25	0.01	0.27	17.60	0.01	0.20	17.41	0.01	0.17	SDSS
4	247.75413	12.77563	17.59	0.01	0.27	16.78	0.01	0.21	16.52	0.01	0.17	SDSS
5	247.77166	12.80192	17.09	0.01	0.26	16.40	0.01	0.20	16.19	0.01	0.16	SDSS
6	247.77027	12.78519	17.65	0.01	0.27	16.98	0.01	0.20	16.77	0.01	0.17	SDSS
7	247.77106	12.78756	18.36	0.01	0.27	17.78	0.01	0.20	17.62	0.01	0.17	SDSS
8	247.73778	12.77706	16.71	0.01	0.27	15.91	0.01	0.20	15.65	0.01	0.17	SDSS
9	247.73598	12.79375	20.41	0.02	0.26	18.97	0.02	0.20	18.39	0.01	0.17	SDSS

[a]See electronic edition for complete data table.

Table 3. Hercules Photometry – Adjacent Fields

Star No.	α (deg J2000.0)	δ (deg J2000.0)	B (mag)	δB (mag)	A_B (mag)	r (mag)	δr (mag)	A_r (mag)	Field No.	SDSS or LBT
0	248.14455	12.72711	18.77	0.01	0.24	17.94	0.01	0.15	1	SDSS
1	248.17113	12.73422	18.53	0.01	0.24	18.02	0.01	0.15	1	SDSS
2	248.15911	12.69833	17.52	0.01	0.25	16.45	0.01	0.15	1	SDSS
3	248.14109	12.71092	20.49	0.02	0.24	18.89	0.02	0.15	1	SDSS
4	248.13436	12.73258	16.44	0.01	0.24	15.51	0.01	0.15	1	SDSS
5	248.12870	12.71724	17.23	0.01	0.24	16.56	0.01	0.15	1	SDSS
6	248.15911	12.69651	20.15	0.01	0.25	18.76	0.01	0.15	1	SDSS
7	248.16960	12.69793	18.84	0.01	0.25	18.13	0.01	0.16	1	SDSS
8	248.15837	12.74721	18.62	0.01	0.24	17.49	0.01	0.15	1	SDSS
9	248.18539	12.70580	19.45	0.01	0.25	18.56	0.01	0.16	1	SDSS

[a]See electronic edition for complete data table.

Table 4.   Hercules structure – parameterized fits

Parameter	Measured	Uncertainty	Bootstrap median
$(m - M)_{Empirical}$	20.625	0.1	20.625
$Distance_{Empricial}$	133.4	6.1	133.4
$(m - M)_{Dotter}$	20.60	0.05	20.60
$Distance_{Dotter}$ (kpc)	131.8	3.0	131.8
$(m - M)_{Girardi}$	20.65	0.1	20.575
$Distance_{Girardi}$	134.9	6.2	130.3
M_V	-5.3	0.4	-5.3
$\mu_{0,V}$	27.7	0.4	27.7
Exponential Profile			
RA (h m s)	16:31:03.00	$\pm 12''$	16:31:02.00
DEC (d m s)	+12:47:13.77	$\pm 5''$	+12:47:13.83
r_h (arcmin)	5.91	0.50	5.97
(pc)	229.3	19.4	231.7
ϵ	0.67	0.03	0.67
θ (degrees)	-72.36	1.65	-72.35
Plummer Profile			
RA (h m s)	16:31:03.12	$\pm 14''$	16:31:03.50
DEC (d m s)	+12:47:14.01	$\pm 6''$	+12:47:15.21
r_h (arcmin)	6.27	0.53	6.17
(pc)	243.3	20.6	239.421
ϵ	0.67	0.03	0.67
θ (degrees)	-72.59	1.72	-72.47
King Profile			
RA (h m s)	16:31:03.22	$\pm 14''$	16:31:02.50
DEC (d m s)	+12:47:14.11	$\pm 6''$	+12:47:14.11
r_c (arcmin)	3.59	0.44	3.80
(pc)	139.3	17.1	147.5
r_t (arcmin)	37.45	8.97	35.25
(pc)	1453.2	348.1	1367.8
ϵ	0.68	0.03	0.68
θ	-72.32	1.70	-72.34

Table 4—Continued

Parameter	Measured	Uncertainty	Bootstrap median

[a]All transverse distances are reported using the $(m - M)_{Empirical} = 20.625$ distance modulus.

[b]Absolute magnitude and central surface brightness are calculated using the exponential profile fit.

Table 5.   Input Hercules 'Nuggets' and Detections

Pointing	No. of stars	M_r	$\mu_{0,r}$	M_B	$\mu_{0,B}$	Peak σ
1	50	-2.9	29.8	-2.2	30.6	2.2
	100	-4.1	28.7	-3.5	29.2	2.0
	150	-4.0	28.8	-3.6	29.2	4.8
	200	-4.5	28.3	-4.3	28.5	6.1
2	50	-3.6	29.2	-2.2	30.6	1.8
	100	-3.7	29.0	-3.3	29.5	3.3
	150	-4.5	28.3	-4.0	28.8	5.3
	200	-4.8	28.0	-4.1	28.7	8.3
3	50	-3.3	29.5	-2.0	30.8	2.1
	100	-3.4	29.4	-3.7	29.1	3.7
	150	-4.4	28.4	-3.5	29.3	7.1
	200	-4.7	28.1	-4.0	28.8	6.9
4	50	-2.6	30.2	-2.8	29.9	1.6
	100	-3.7	29.1	-3.1	29.7	3.8
	150	-4.5	28.3	-3.6	29.2	4.0
	200	-4.9	27.9	-4.1	28.7	9.0

[a]All nuggets have an exponential profile with half light radius of 3 arcminutes.

Table 6.   Representative orbital parameters for Hercules

Case	$V_{GSR,rad}$ (km s^{-1})	$V_{GSR,tan}$ (km s^{-1})	R_{peri} (kpc)	R_{apo} (kpc)	T (Gyr)	e	Inclination degree	μ_α (marcsec/cent)	μ_δ (marcsec/cent)
1	142	20	5	167	2.2	0.95	83	-19.64	-24.2
2	141	50	13	168	2.3	0.86	89	-15.11	-25.7
3	140	105	36	176	2.6	0.66	92	-6.83	-28.3
4	137	204	86	245	4.0	0.48	93	8.23	-33.1
5	143	11	3	167	2.2	0.97	135	-21.18	-21.24
6	144	40	11	169	2.3	0.88	141	-19.74	-16.71
7	146	95	32	179	2.6	0.70	141	-17.11	-8.43
8	150	195	79	249	4.0	0.52	141	-12.32	6.63